The Astrophysical Journal, 889:137 (20pp), 2020 February 1 https://doi.org/10.3847/1538-4357/ab6596

Balmer Break Galaxy Candidates at $z \sim 6$: A Potential View on the Star Formation Activity at $z \gtrsim 14$

Ken Mawatari[1,2], Akio K. Inoue[2,3,4], Takuya Hashimoto[2,5,6,7], John Silverman[8], Masaru Kajisawa[9], Satoshi Yamanaka[2,4], Toru Yamada[10,11], Iary Davidzon[12], Peter Capak[12,13], Lihwai Lin[14], Bau-Ching Hsieh[14], Yoshiaki Taniguchi[15], Masayuki Tanaka[6], Yoshiaki Ono[1], Yuichi Harikane[1,6], Yuma Sugahara[1,16], Seiji Fujimoto[1], and Tohru Nagao[9]

[1] Institute for Cosmic Ray Research, The University of Tokyo, Kashiwa, Chiba 277-8582, Japan; mawatari@icrr.u-tokyo.ac.jp
[2] Department of Environmental Science and Technology, Faculty of Design Technology, Osaka Sangyo University, 3-1-1, Nakagaito, Daito, Osaka, 574-8530, Japan
[3] Department of Physics, School of Advanced Science and Engineering, Waseda University, 3-4-1, Okubo, Shinjuku, Tokyo 169-8555, Japan
[4] Waseda Research Institute for Science and Engineering, 3-4-1, Okubo, Shinjuku, Tokyo 169-8555, Japan
[5] Faculty of Science and Engineering, Waseda University, 3-4-1, Okubo, Shinjuku, Tokyo 169-8555, Japan
[6] National Astronomical Observatory of Japan, Osawa 2-21-1, Mitaka, Tokyo 181-8588, Japan
[7] Tomonaga Center for the History of the Universe (TCHoU), Faculty of Pure and Applied Sciences, University of Tsukuba, Tsukuba, Ibaraki 305-8571, Japan
[8] Kavli Institute for the Physics and Mathematics of the Universe, The University of Tokyo, Kashiwa, Chiba 277-8583, Japan
[9] Research Center for Space and Cosmic Evolution, Ehime University, 2-5 Bunkyo-cho, Matsuyama, Ehime 790-8577, Japan
[10] Institute of Space Astronautical Science, Japan Aerospace Exploration Agency, Sagamihara, Kanagawa 252-5210, Japan
[11] Astronomical Institute, Tohoku University, Aoba, Aramaki, Aoba-ku, Sendai, Miyagi, 980-8578, Japan
[12] Infrared Processing and Analysis Center, California Institute of Technology, MC 100-22, 770 S. Wilson Avenue, Pasadena, CA 91125, USA
[13] California Institute of Technology, MC 105-24, 1200 E. California Boulevard, Pasadena, CA 91125, USA
[14] Institute of Astronomy & Astrophysics, Academia Sinica, Taipei 106, Taiwan
[15] The Open University of Japan, 2-11 Wakaba, Mihama-ku, Chiba 261-8586, Japan
[16] Department of Physics, Graduate School of Science, The University of Tokyo, 7-3-1 Hongo, Bunkyo, Tokyo, 113-0033, Japan
Received 2019 June 28; revised 2019 December 20; accepted 2019 December 23; published 2020 February 3

Abstract

We search for galaxies with a strong Balmer break (Balmer break galaxies; BBGs) at $z \sim 6$ over a 0.41 deg^2 effective area in the COSMOS field. Based on rich imaging data, including data obtained with the Atacama Large Millimeter/submillimeter Array (ALMA), three candidates are identified by their extremely red K–[3.6] colors, as well as by nondetection in the X-ray, optical, far-infrared, and radio bands. The nondetection in the deep ALMA observations suggests that they are not dusty galaxies but BBGs at $z \sim 6$, although contamination from active galactic nuclei at $z \sim 0$ cannot be completely ruled out for the moment. Our spectral energy distribution analyses reveal that the BBG candidates at $z \sim 6$ have stellar masses of $\approx 5 \times 10^{10}\,M_\odot$ dominated by old stellar populations with ages of $\gtrsim 700$ Myr. Assuming that all three candidates are real BBGs at $z \sim 6$, we estimate the stellar mass density to be $2.4^{+2.3}_{-1.3} \times 10^4\,M_\odot$ Mpc^{-3}. This is consistent with an extrapolation from the lower-redshift measurements. The onset of star formation in the three BBG candidates is expected to be several hundred million yr before the observed epoch of $z \sim 6$. We estimate the star formation rate density (SFRD) contributed by progenitors of the BBGs to be 2.4–12 $\times 10^{-5}\,M_\odot$ yr^{-1} Mpc^{-3} at $z > 14$ (99.7% confidence range). Our result suggests a smooth evolution of the SFRD beyond $z = 8$.

Unified Astronomy Thesaurus concepts: Galaxy formation (595); Early universe (435); Star formation (1569); High-redshift galaxies (734)

1. Introduction

Star formation is the most fundamental process in galaxy formation and evolution. It is important to investigate the cosmic star formation rate density (SFRD) at a wide redshift range because its evolution can trace cosmic star formation history (SFH). The SFRD has been measured up to $z = 10$ (e.g., Hopkins & Beacom 2006; Oesch et al. 2013; Madau & Dickinson 2014; Bouwens et al. 2015; Rowan-Robinson et al. 2016; Ishigaki et al. 2018). There is a general consensus that the SFRD increases from $z = 0$ to ~2–3 and then monotonically decreases up to $z \sim 8$. The monotonic decrease at $3 < z < 8$ is well expressed by a simple power-law function, $\rho_{\rm SFR} \propto (1+z)^{\alpha}$, whereas there is a small variation in the slope among different studies (Madau & Dickinson 2014; Finkelstein et al. 2015a; McLeod et al. 2016; Oesch et al. 2018; Bhatawdekar et al. 2019).

At $z \gtrsim 8$, however, the evolution of the cosmic SFRD is still controversial, which seems to be due to the observational limitations of current instruments such as the *Hubble Space Telescope* (*HST*). A smooth evolution from $z \sim 5$ to ~10 with $-2.6 \leqslant \alpha \leqslant -5.8$ is suggested by Finkelstein et al. (2015a), McLeod et al. (2016), and Bhatawdekar et al. (2019; see also Ellis et al. 2013 and Kikuchihara et al. 2019). In contrast, an accelerated evolution at $z \gtrsim 8$ is suggested by Bouwens et al. (2011) and Oesch et al. (2012, 2014, 2018), in which the power-law slope dramatically changes from $\alpha \approx -4$ at $z < 8$ to $\alpha = -10.9$ at $8 < z \lesssim 10$. Oesch et al. (2018) claimed that the rapid decline of SFRD beyond $z \approx 8$ is naturally explained by the number density evolution of dark matter halos. This explanation is also supported by Harikane et al. (2018), who reproduced the rapid SFRD decrease assuming no redshift dependence on a tight relation among the halo mass, SFR, and dark matter accretion rate. To obtain a definitive conclusion, significant improvements on the SFRD measurements at $z > 8$ are required.

If galaxies experience passive evolution with little or no star formation activity for more than several hundred million yr, their spectra are dominated by A-type or cooler stars with a Balmer/4000 Å break (e.g., Leitherer et al. 1999; Wiklind et al. 2008).

Studying passive or Balmer break galaxies (BBGs; Wiklind et al. 2008) at high redshift can potentially help explore a redshift frontier of cosmic SFH because such galaxies should have undergone intense star formation a long time before they were observed. For example, a spectroscopically confirmed galaxy at $z = 9.1$ has a strong Balmer break (Hashimoto et al. 2018), whereas this galaxy also shows current star formation and cannot be regarded as a pure passive galaxy. Hashimoto et al. (2018) analyzed the spectral energy distribution (SED), concluding that the galaxy started star formation at redshifts as high as $z \sim 15$. Because the $z = 9.1$ galaxy was first selected by the standard Lyman break technique and its Balmer break was found serendipitously, we cannot obtain any statistical quantities for such galaxies showing the Balmer break. A systematic survey of BBGs at high-z, namely $z > 5$, is significantly interesting to investigate the cosmic star formation at $z > 10$.

Passive galaxies have been well investigated at $z < 3$, which reveals that the number density of the passive galaxies decreases with increasing redshift (Domínguez Sánchez et al. 2011; Kajisawa et al. 2011; Muzzin et al. 2013; Davidzon et al. 2017). At $z > 3$, the Balmer break is shifted to $\lambda > 1.5\,\mu$m, making detection of passive galaxies challenging. The redshift record of spectroscopically confirmed passive galaxies reaches as large as $z \approx 4$ (Glazebrook et al. 2017; Tanaka et al. 2019). Even at larger redshifts of $4 \lesssim z \lesssim 6$, the number of photometric BBG candidates increases because of the extremely deep and wide near-infrared (NIR) survey data (Rodighiero et al. 2007; Wiklind et al. 2008; Mancini et al. 2009; Huang et al. 2011; Caputi et al. 2012; Nayyeri et al. 2014; Merlin et al. 2019; Santini et al. 2019). Mawatari et al. (2016) proposed a color selection scheme to isolate BBGs at $5 \lesssim z \lesssim 8$ and identified three candidates in the *Spitzer* Extended Deep Survey (SEDS; Ashby et al. 2013) UDS field.

In most previous studies on photometric identification of high-z BBGs, there still remains possible contamination from dusty galaxies (DGs) with a similar red rest-frame optical color to the BBGs (e.g., Brammer et al. 2009). This is due to the lack of a sufficiently deep constraint on dust emission in the mid-infrared (MIR) to far-infrared (FIR) regions. The passive galaxy at $z \sim 6.5$ reported in the pioneering work by Mobasher et al. (2005) was later identified as a dusty contaminant at $z < 3$ detected with *Spitzer*/MIPS (Dunlop et al. 2007). One of the three BBG candidates reported by Mawatari et al. (2016; object ID: SEDS_UDS_BBG-34) was found to be a low-z DG because of detections in the new FIR imaging data from the SCUBA-2 Cosmology Legacy Survey (S2CLS; Geach et al. 2017) and the Atacama Large Millimeter/submillimeter Array (ALMA) SCUBA-2 UDS survey (AS2UDS; Stach et al. 2019). ALMA may be the only instrument that can offer critical data to resolve the degeneracy between passive and dusty red galaxies because of its unprecedented sensitivity and spatial resolution (Schreiber et al. 2018; Santini et al. 2019).

In this work, we apply a color selection of BBGs to the deep and wide-area imaging data available in an effective area of 0.41 deg^2 in the COSMOS field. We further conduct ALMA observations to remove contamination from DGs. This study is structured as follows. The imaging data used in this work are summarized in Section 2. Spectral templates of galaxies and active galactic nuclei (AGNs) to tune the color selection criteria and analyze the SEDs are described in Section 3. In Sections 4 and 5, we describe the selection of $5 \lesssim z \lesssim 8$ BBG candidates and follow-up observations with ALMA. In Sections 6 and 7, we discuss the sample significance through SED analyses and implications of their progenitors' SFRD. We use the AB magnitude system (Oke & Gunn 1983) and adopt a cosmology with $H_0 = 70.4\,\mathrm{km\,s^{-1}\,Mpc^{-1}}$, $\Omega_M = 0.272$, and $\Omega_\Lambda = 0.728$ (Komatsu et al. 2011).

2. Multiband Imaging Data

We gathered the multiband photometric data available in the COSMOS field. In Table 1, we present the instruments, filters, FWHM of the point-spread function (PSF), limiting flux, survey name, and references. Figure 1 shows the spatial coverage of each set of data. In the following section, we explain each data set.

We use deep *Spitzer* Infrared Array Camera (IRAC; Fazio et al. 2004) images at wavelengths of 3.6 and 4.5 μm from the *Spitzer* Large Area survey with Hyper Suprime-Cam (SPLASH; PI: P. Capak; Laigle et al. 2016). Ground-based *Y*-, *J*-, *H*-, and *K*-band images were also available from the UltraVISTA survey (McCracken et al. 2012). We used only the deepest data in the four ultradeep (UD) stripes that are included in the third data release (DR3[17]). We call these stripes UVISTA UD stripes 1, 2, 3, and 4 (Figure 1). These stripes cover $\sim$0.66 deg^2 in the SPLASH field.

There are *HST* Advanced Camera for Surveys (ACS) F814W imaging data taken in the original COSMOS *HST* Treasury project (hereafter *HST*-COSMOS; Koekemoer et al. 2007; Scoville et al. 2007). The F814W-band image and catalog were downloaded from the COSMOS website.[18] The *HST*-COSMOS data cover the UVISTA UD stripes, except for the westernmost stripe 4. Other optical imaging data at the *g*, *r*, *i*, *z*, and *y* bands are available from the Subaru strategic program using the Hyper Suprime-Cam (HSC-SSP; Aihara et al. 2018; Furusawa et al. 2018; Kawanomoto et al. 2018; Komiyama et al. 2018; Miyazaki et al. 2018). We used the HSC-SSP public data (PDR2 or S18A; Aihara et al. 2019) in the deepest UD layer that covers UVISTA UD stripes 1–3.

At the MIR wavelength range, IRAC 5.8 and 8.0 and MIPS 24 and 70 μm band imaging data are available from the *Spitzer* COSMOS survey (S-COSMOS; Sanders et al. 2007; Frayer et al. 2009; Le Floc'h et al. 2009). These *Spitzer* MIR data[19] cover the all four UVISTA UD stripes, while the depth in the westernmost UVISTA UD stripe 4 is shallow.

There are two major FIR surveys conducted by ESA's *Herschel* space observatory (Pilbratt et al. 2010). One is the Photodetector Array Camera and Spectrometer (PACS; Poglitsch et al. 2010) Evolutionary Probe (PEP; Lutz et al. 2011) survey. We used the 100 and 160 μm band images and catalogs from the PEP first data release (DR1[20]). These images cover the four UVISTA UD stripes, except for a part of the westernmost stripe 4. Another survey is the *Herschel* Multi-Tiered Extragalactic Survey (HerMES; Oliver et al. 2012), which uses the Spectral and Photometric Imaging Receiver (SPIRE; Griffin et al. 2010) at wavelengths of 250, 350, and 500 μm. We obtained the SPIRE images and catalogs in the COSMOS field from the fourth HerMES data release (DR4)

[17] http://ultravista.org/release3/
[18] http://cosmos.astro.caltech.edu/page/hst
[19] http://cosmos.astro.caltech.edu/page/spitzer
[20] http://www.mpe.mpg.de/ir/Research/PEP/DR1

Table 1
COSMOS Data Set

Instrument	Filter	FWHM[a] (arcsec)	Limiting Flux[b]	Survey	Reference[c]
(1)	(2)	(3)	(4)	(5)	(6)
HST/ACS	F814W	0.10	27.5(26.6[d]) mag	*HST*-COSMOS	(1), (2)
Subaru/HSC	*g*	0.79	27.3 mag	HSC-SSP/UD S18A	(3)
Subaru/HSC	*r*	0.66	27.3 mag	HSC-SSP/UD S18A	(3)
Subaru/HSC	*i*	0.64	27.1 mag	HSC-SSP/UD S18A	(3)
Subaru/HSC	*z*	0.58	26.8 mag	HSC-SSP/UD S18A	(3)
Subaru/HSC	*y*	0.70	25.8 mag	HSC-SSP/UD S18A	(3)
VISTA/VIRCAM	*Y*	0.8	25.8 mag	UltraVISTA/UD DR3	(4)
VISTA/VIRCAM	*J*	0.77	25.7 mag	UltraVISTA/UD DR3	(4)
VISTA/VIRCAM	*H*	0.75	25.5 mag	UltraVISTA/UD DR3	(4)
VISTA/VIRCAM	K_s	0.75	25.2 mag	UltraVISTA/UD DR3	(4)
Spitzer/IRAC	3.6 μm	1.7	23.9 mag	SPLASH	(5), (6)
Spitzer/IRAC	4.5 μm	1.6	24.0 mag	SPLASH	(5), (6)
Spitzer/IRAC	5.8 μm	1.8	20.8 mag	S-COSMOS	(7)
Spitzer/IRAC	8.0 μm	2.1	20.7 mag	S-COSMOS	(7)
Spitzer/MIPS	24 μm	5.9	19.0 mag	S-COSMOS	(8)
Spitzer/MIPS	70 μm	18.6	14.1 mag	S-COSMOS	(9)
Herschel/PACS	100 μm	7.2	14.2 mag	PEP DR1	(10)
Herschel/PACS	160 μm	12.0	13.4 mag	PEP DR1	(10)
Herschel/SPIRE	250 μm	18.15	12.9 mag	HerMES DR4	(11), (12)
Herschel/SPIRE	350 μm	25.15	12.6 mag	HerMES DR4	(11), (12)
Herschel/SPIRE	500 μm	36.3	12.7 mag	HerMES DR4	(11), (12)
JCMT/SCUBA-2	850 μm	8.0	14.1 mag	S2CLS	(13)
VLA	1.4 GHz	1.5 × 1.4	75 μJy	VLA-COSMOS/Large	(14)
VLA	3 GHz	0.75	11.5 μJy	VLA-COSMOS/Large	(15)
XMM-Newton	0.5–2 keV	⋯	1.0×10^{-15} erg cm^{-2} s^{-1}	*XMM*-COSMOS	(16)
XMM-Newton	2–10 keV	⋯	5.6×10^{-15} erg cm^{-2} s^{-1}	*XMM*-COSMOS	(16)
XMM-Newton	5–10 keV	⋯	1.1×10^{-14} erg cm^{-2} s^{-1}	*XMM*-COSMOS	(16)
Chandra	0.5–2 keV	⋯	4.9×10^{-16} erg cm^{-2} s^{-1}	*Chandra*-COSMOS Legacy	(17)
Chandra	2–10 keV	⋯	3.1×10^{-15} erg cm^{-2} s^{-1}	*Chandra*-COSMOS Legacy	(17)
Chandra	0.5–10 keV	⋯	1.9×10^{-15} erg cm^{-2} s^{-1}	*Chandra*-COSMOS Legacy	(17)

Notes.
[a] The FWHMs are estimated by stacking 100–200 bright stars in the survey area for *HST*, Subaru/HSC, VISTA/VIRCAM, and *Spitzer*/IRAC images. The FWHMs for *Spitzer*/MIPS and *Herschel* are quoted from reference literature (Lutz et al. 2011; Andrews et al. 2017). The instrumental beam size is shown for the JCMT/SCUBA-2 image.
[b] The 5σ limiting magnitudes are measured adopting 2 × PSF (FWHM) diameter apertures and an aperture correction for *HST*, Subaru/HSC, VISTA/VIRCAM, and *Spitzer*/IRAC images. For *Spitzer*/MIPS, *Herschel*/PACS, JCMT/SCUBA-2, and VLA images, 5σ limiting magnitudes or flux densities from the references are shown. For the *Herschel*/SPIRE images that severely suffer from source confusion, the confusion limits estimated in Oliver et al. (2012) are listed. For *XMM-Newton* and *Chandra* data, limiting fluxes achieved over 50% of the survey area are adopted from the references.
[c] (1) Koekemoer et al. (2007), (2) Scoville et al. (2007), (3) Aihara et al. (2019), (4) McCracken et al. (2012), (5) PI: P. Capak, (6) Laigle et al. (2016), (7) Sanders et al. (2007), (8) Le Floc'h et al. (2009), (9) Frayer et al. (2009), (10) Lutz et al. (2011), (11) Oliver et al. (2012), (12) Andrews et al. (2017), (13) Geach et al. (2017), (14) Schinnerer et al. (2007), (15) Smolčić et al. (2017), (16) Cappelluti et al. (2009), (17) Civano et al. (2016).
[d] A 5σ limiting magnitude estimated with 0.″6 diameter apertures that are actually used in this work.

through the *Herschel* Database in Marseille (HeDaM[21]) operated by CeSAM and hosted by the Laboratoire d'Astrophysique de Marseille. The Submillimeter Common-User Bolometer Array-2 (SCUBA-2; Holland et al. 2013) equipped with the James Clerk Maxwell Telescope (JCMT) provides similarly deep FIR images to the *Herschel* images but better spatial resolution. We used the SCUBA-2 850 μm map of the COSMOS field taken as a part of the S2CLS[22] (Geach et al. 2017). This S2CLS 850 μm map covers the four UVISTA UD stripes, except for a part of the westernmost stripe 4. We note that the S2CLS 850 μm map is inhomogeneous, and the easternmost UVISTA UD stripe 1 falls into a shallow area. Fortunately, this does not affect this work because no BBG candidate is found there.

There are rich radio and X-ray data available in the COSMOS field. Homogeneously deep 1.4 and 3 GHz maps were provided by the Karl G. Jansky Very Large Array (VLA) COSMOS large project (Schinnerer et al. 2007; Smolčić et al. 2017). We used the catalogs[23] of ∼2400 and ∼11,000 sources with a signal-to-noise ratio larger than five (S/N > 5) in the 1.4 and 3 GHz maps, respectively. In the X-ray, both the *XMM-Newton* and *Chandra* satellites observed the ∼2 deg^2 area in the *XMM*-COSMOS survey (Cappelluti et al. 2009) and *Chandra*-COSMOS legacy survey (Civano et al. 2016). We used the *XMM*-COSMOS catalog of ∼1800 sources and the

[21] http://hedam.lam.fr/HerMES/index/dr4
[22] https://doi.org/10.5281/zenodo.57792
[23] http://cosmos.astro.caltech.edu/page/radio

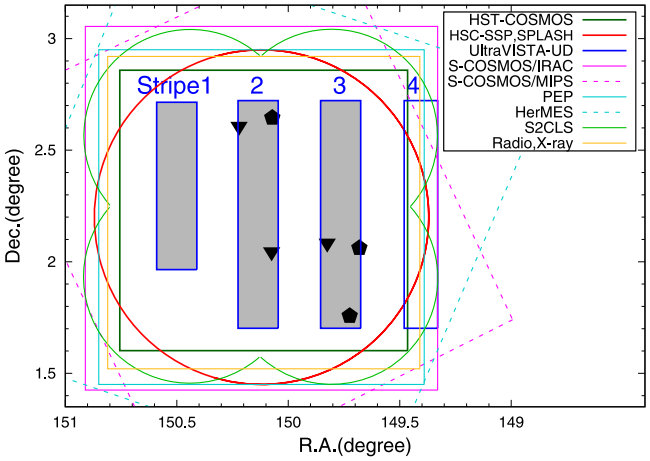

Figure 1. Sky coverage of the survey data used in this work: *HST*-COSMOS (dark green box), HSC-SSP UD and SPLASH (red circle), UltraVISTA UD (blue boxes), S-COSMOS (magenta solid box for the IRAC 5.8 and 8.0 μm and magenta dashed box for the MIPS 24 and 70 μm), PEP (cyan solid box), HerMES (cyan dashed box), S2CLS (light green curve), and VLA-COSMOS, *XMM*-COSMOS, and *Chandra*-COSMOS Legacy (yellow box). The blue numbers are assigned for the four UltraVISTA UD stripes. The area where we searched for BBGs at $5 \lesssim z \lesssim 8$ is emphasized by the gray shading. The observed BBG candidates with and without ALMA detection (see Section 5) are shown by triangles and pentagons, respectively.

Chandra-COSMOS legacy catalog of ∼4000 sources from the COSMOS website.[24]

In summary, we analyzed UVISTA UD stripes 1, 2, and 3, where the above multiwavelength imaging data were homogeneously deep.

3. Template Colors

Because the Balmer break at $z > 5$ is redshifted to an observed wavelength longer than the K band, the main color selection criterion is red $K-[3.6]$ to capture the break. In addition, we set a secondary color selection criterion of $[3.6]-[4.5]$ to reject the DGs showing similar red K–[3.6] colors. To make a suitable set of the color selection criteria for $z \sim 6$ BBGs, Mawatari et al. (2016) investigated the galaxy colors on the $K-[3.6]$ versus $[3.6]-[4.5]$ two-color diagram with SED model templates. In this section, we present an updated set of the color selection criteria for $z \sim 6$ BBGs based on an expanded analysis of the model template colors.

3.1. Galaxy Model: Star+Nebular+Dust

Our galaxy SED models consist of three components: the stellar continuum models (Bruzual & Charlot 2003), the nebular emission models (Inoue 2011), and the empirical dust emission templates (Rieke et al. 2009). We call them "Star +Nebular+Dust." These models were also used in our previous studies (Hashimoto et al. 2018, 2019; Tamura et al. 2019). For the stellar continuum models, we assume a Chabrier initial mass function (IMF; Chabrier 2003) with lower and upper mass cutoffs of 0.1 and 100 $M_\odot$, respectively. The SFH is assumed to be either a constant SFR or exponentially declining/rising with various e-folding timescales. The parameter ranges for age ($T_{\rm age}$), metallicity (Z), and e-folding timescale ($\tau_{\rm SFH}$) are as follows: 1 Myr $< T_{\rm age} <$ the cosmic age at a given redshift, $0.0001 < Z < 0.02$, and 0.01 Gyr $\leqslant \tau_{\rm SFH} \leqslant$ 10 Gyr.

The nebular continuum and emission line fluxes are calculated from the ionizing photon production rate and metallicity of the stellar components (Bruzual & Charlot 2003) in the same manner as Inoue (2011). The escape fraction of ionizing photons is assumed to be zero. Fluxes at rest-frame wavelengths equal to or shorter than Lyα are attenuated by the intergalactic medium (IGM), following the analytic model of Inoue et al. (2014). For dust attenuation, A_V, we apply the same amount to both nebular and stellar continua, assuming the Calzetti law (Calzetti et al. 2000). We also put the maximum A_V as a function of SFR, $A_V < \max(4 \times {\rm SFR}^{0.3}, 3.5)$, to avoid the templates of extremely dusty and passive galaxies never observed so far (see discussion in Appendix A).

The energy attenuated by dust is reradiated in the infrared wavelengths ($5\,\mu{\rm m} \lesssim \lambda \lesssim 1000\,\mu{\rm m}$). The dust emission is described by empirical templates of nearby infrared-bright galaxies (Rieke et al. 2009) as a function of the total infrared luminosity ($L_{\rm IR}$). We selected the template with $L_{\rm IR}$ equal to the luminosity attenuated by dust.

3.2. AGN Templates

Our AGN template set consists of nine empirical and 24,000 theoretical spectra. The empirical templates are taken from the SWIRE template library (Polletta et al. 2007): three type 1 AGNs (QSO1, TQSO1, and BQSO1), four type 2 AGNs (Sey2, Sey1.8, QSO2, and Torus), and two starburst galaxies with AGNs (Mrk231 and I19254). Because all of them are constructed based on various types of observed AGNs, their spectra include the host galaxy contribution.

The theoretical AGN templates were constructed by Fritz et al. (2006) and Feltre et al. (2012) based on comprehensive modeling of a dusty torus around a black hole (BH). Their model (hereafter "TORUS") has realistic torus geometry parameterized by an outer-to-inner radial ratio, an opening angle, a gas density profile, an optical depth at the equatorial plane, and a viewing angle. Following the unified AGN picture (Antonucci 1993; Urry & Padovani 1995), we consider type 1 and 2 AGNs depending on the viewing angle. Fritz et al. (2006) mentioned that not only the torus emission but also the contribution from the host galaxy are needed to reproduce the actual observed SEDs of AGNs, except for a few cases of type 1 AGNs (see also discussion in Section 7.1.1).

3.3. Expected Colors for $z \sim 6$ BBGs

We investigated the colors of the Star+Nebular+Dust galaxy models of $0 < z < 8$ and $0 \leqslant A_V \leqslant 6$. We adopted the same setting for $T_{\rm age}$ and Z as described in Section 3.1. Here we only considered the exponentially declining SFH with 0.01 Gyr $\leqslant \tau_{\rm SFH} \leqslant$ 10 Gyr to devise the BBG selection criteria. There are three types of galaxies that show extremely red K–[3.6] colors: (1) passive galaxies dominated by old stars (BBGs) at $z \gtrsim 5$, (2) DGs at $z > 1$, and (3) extremely young dusty star-forming galaxies with strong nebular emission lines (dusty nebular line emitters; DNLEs) at $z > 4$. Example spectra of these models are shown in Figure 2. The Balmer break and dust attenuation make red K–[3.6] colors for BBGs and DGs, respectively. For DNLEs, strong emission lines such as Hα at $z \sim 4.5$ and [O III] 5007 at $z \sim 6.5$ boost the [3.6]-band flux.

[24] http://cosmos.astro.caltech.edu/page/xray

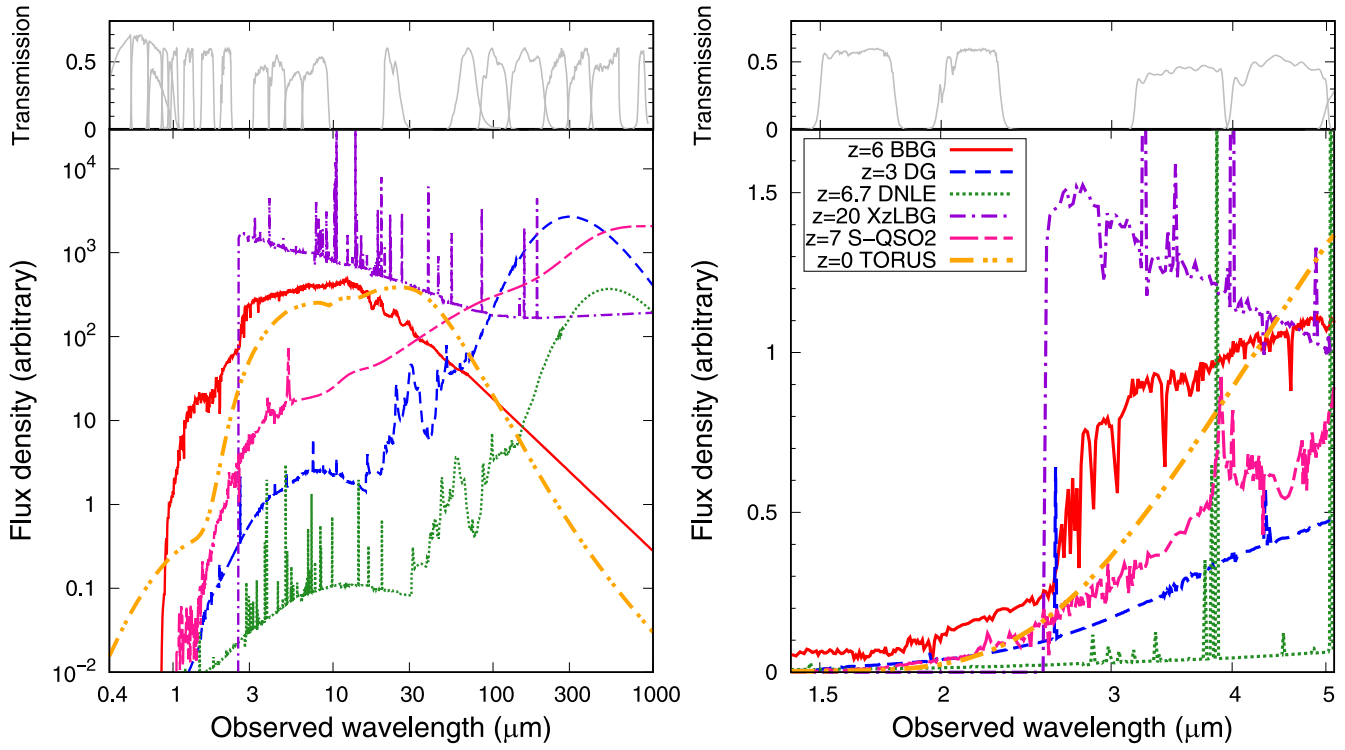

Figure 2. Example spectra of the galaxy and AGN templates with extremely red K–[3.6] but flat [3.6]–[4.5] colors. The left and right panels show the same spectra, whereas in the right panel, the flux is in the linear scale and the wavelength range is limited to the NIR regime. Four types of galaxies come from the Star+Nebular +Dust model library: a passive galaxy at $z = 6$ with $A_V = 0$ (BBG), a DG at $z = 3$ with $A_V = 4$ (DG), an extremely young DG with strong nebular emission lines at $z = 6.7$ with $A_V = 2$ (DNLE), and an LBG at $z = 20$ with $A_V = 0$ (XzLBG). Two AGN spectra come from the empirical and theoretical AGN template library: a type 2 QSO template of the SWIRE template library at $z = 7$ (S-QSO2) and a heavily obscured dust torus model at $z = 0$ (TORUS). We arbitrarily scaled the individual spectra for display purposes. The filter response curves used in this work are shown in the top panels.

The left panel of Figure 3 shows the Star+Nebular+Dust model tracks on the K–[3.6] versus [3.6]–[4.5] two-color diagram, from which we define the BBG color criteria as

$$K - [3.6] > 1.75, \quad (1)$$

$$K - [3.6] > 2.4([3.6]-[4.5]) + 1.05. \quad (2)$$

These color criteria are a slightly modified version of those in a previous study (Mawatari et al. 2016) to select BBGs with $T_{\rm age} \gtrsim 0.3$ Gyr.

At $z < 4$, a rest-frame $U - V$ and $V - J$ color selection method (rest-UVJ selection; Williams et al. 2009) is often used to select BBGs. Based on the model template colors, we found that our BBG selection samples $\sim$0.1 Gyr younger galaxies than the rest-UVJ selection. We neglect this small difference between the selection methods when comparing our results with other studies (Section 7). We also confirmed that stars in the Milky Way (MW) do not satisfy the color criteria (Mawatari et al. 2016).

As can be seen in the left panel of Figure 3, DGs and DNLEs can contaminate our BBG selection criteria. The DGs and DNLEs can be removed by dust emission in FIR. The BBGs are dust-poor and much bluer in NIR–FIR color than DGs and DNLEs. In the right panel of Figure 3, we show [3.6]–[850] colors (i.e., NIR–FIR colors) of the Star+Nebular+Dust model galaxies.[25] The [3.6]–[850] colors of BBGs are clearly different from others, as expected.

Additionally, we note an interesting possibility that our BBG criteria can identify Lyman break galaxies (LBGs) at extremely high redshift (extremely high-z LBGs; XzLBGs). In Figure 3, the XzLBG color tracks at $z > 10$ are superposed based on a Stellar+Nebular+Dust model with $Z = 0.004$, $T_{\rm age} < \tau_{\rm SFH}$, and $A_V = 0$. The XzLBGs at $17.5 \lesssim z \lesssim 30$ satisfy the BBG criteria. An example spectrum of the XzLBG models is also shown in Figure 2.

We also investigated the colors of the AGN templates. We found that our BBG color criteria can be satisfied by the SWIRE QSO2 template at $z \sim 7$, as well as by some type 2 TORUS templates at $z \lesssim 1$ and $\sim$8 (left panel of Figure 4). Their spectra are also shown in Figure 2. In the SWIRE QSO2 case, the red K–[3.6] color can be achieved by a combination of the heavily obscured continuum and broad [O III] 5007 emission line around 3.6 μm. In the TORUS model case, torus continuum emission alone can mimic the BBG-like color. Among these AGN contaminations, the SWIRE QSO2-type objects can be removed by their bright FIR emission (right panel of Figure 4). In contrast, some of the TORUS contaminations have blue [3.6]–[850] color, which makes it hard to distinguish them from the BBGs at $z \gtrsim 5$. However, such AGNs with very little contribution from the host galaxies to the whole SED would be extreme and rare, as we discuss later (Section 7.1.1).

4. Selection of BBG Candidates

In this section, we present the selection procedure of BBG candidate galaxies from the multiwavelength data in the COSMOS field. First, we select BBG candidates on the

[25] Here we fix [3.6] = 24 mag, which is almost the same as the observed magnitudes for our final BBG sample (Section 4 and Table 2), to calculate the model's $L_{\rm IR}$ and then 850 μm magnitude.

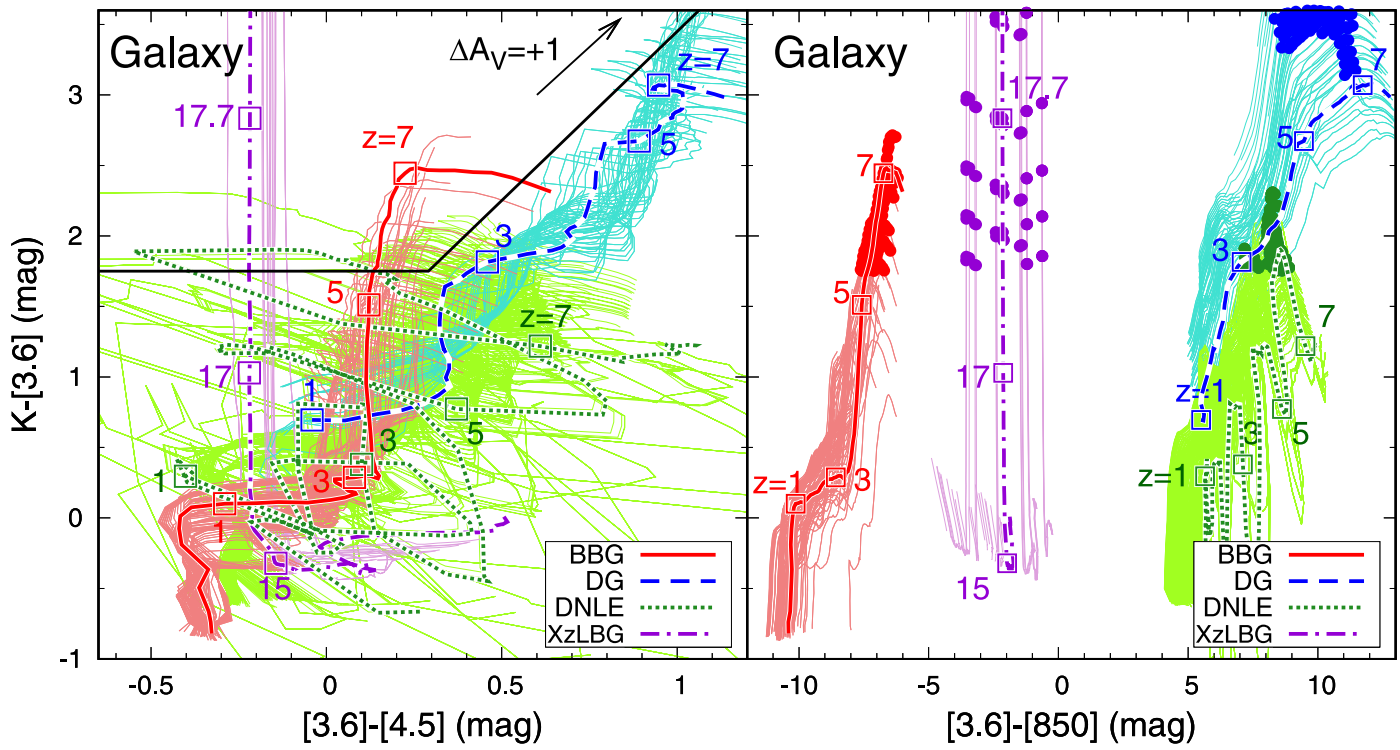

Figure 3. Star+Nebular+Dust model galaxy tracks from $z = 0$ to 8 (or redshift when the age of the universe is equal to the model age) on two-color diagrams of K–[3.6] vs. [3.6]–[4.5] (left panel) and [3.6]–[850] (right panel). The BBGs, DGs, DNLEs, and XzLBGs are shown by the red, blue, green, and violet curves, respectively. For display purposes, we limited the dust attenuation to $A_V = 0$ (BBGs and XzLBGs), 4 (DGs), and 2 (DNLEs). The black arrow indicates the dust reddening effect in the case of $\Delta A_V = +1$. The thick curves are characteristic examples of each type of model galaxies shown in Figure 2, where some redshifts are emphasized by squares. In the left panel, the BBG color criteria described in Equations (1) and (2) are shown by the solid black line. In the right panel, the models satisfying the BBG color criteria are shown by the filled circles.

K–[3.6] versus [3.6]–[4.5] two-color diagram (Section 4.1). Then, we narrow down the candidates to six that are not detected in the X-ray, FIR, and radio bands, as well as the optical bands (Section 4.2).

4.1. NIR Color Selection

Source extraction was performed on the SPLASH [3.6]-band image using SExtractor (Bertin & Arnouts 1996) version 2.5.0. We masked areas around objects brighter than 20 mag in [3.6] to remove faint objects whose photometry was affected by the bright objects. The masked area of each bright object was defined by the isophotal level at twice the sky fluctuation in the [3.6]-band image. Avoiding the masked region, the effective area was 0.41 deg^2. We focused on isolated sources within a 3″ radius not only in the [3.6]-band image but also in the K- and [4.5]-band images. Namely, we selected sources that do not have any nearby objects brighter than 10% of their flux density in all three bands within the circular area. We found ∼37,000 such isolated objects down to [3.6] ≈ 24.1 mag (4σ) and called them the parent sample.

We estimated the completeness of our source extraction by detecting artificial sources randomly embedded in the [3.6]-band image. Following Barmby et al. (2008) and Ashby et al. (2013), we considered that an artificial object is recovered if the object is detected within 1″ from the input position and its measured flux density is within a 50% difference from the priori flux density. We further adopted the isolation criterion to match the parent sample construction. The resultant completeness as a function of the input artificial objects' magnitude is shown in Figure 5. We could detect objects brighter than ∼24 mag with completeness higher than 50%.

In photometry, we used the task PHOT in IRAF, where aperture diameters were set to 2× the FWHM of PSFs in every band image. The photometric aperture is centered at the detection position in each band. If no object was detected in the K- or [4.5]-band images within 1″ from the [3.6]-band detected position, the photometric aperture was forced to be centered at the [3.6]-band position. The aperture magnitudes were corrected to the total magnitudes using aperture correction factors estimated for point sources. For the photometric uncertainty, we measured 1σ of the distribution of random aperture photometry in each image and applied the same aperture correction. We neglected the Galactic extinction for the K, [3.6], and [4.5] photometry because it is very small (<0.01 mag; Schlegel et al. 1998 with $R_V = 3.1$).

We applied the BBG color criteria (Equations (1) and (2)) to the parent sample down to ≈24.1 mag corresponding to the 4σ limiting magnitude in the [3.6] band. In the case of nondetection ($<2\sigma$) in the K and [4.5] bands, we put the lower and upper limits on their K–[3.6] and [3.6]–[4.5] colors with the 2σ limiting magnitudes, respectively. We identified 23 objects satisfying the BBG color criteria, which are referred to as the color-selected sample in the following sections.

4.2. Multiband Selection

We constructed a multiband photometry catalog for the color-selected sample. For the photometry at wavelengths between 0.4 and 10 μm, we measured the total magnitudes ourselves in the same manner as adopted for the K-, [3.6]-, and [4.5]-band images. Here we used 2× PSF apertures for all bands but the F814W band. For the F814W-band photometry, larger (0.″6 diameter) apertures were used to avoid flux loss by

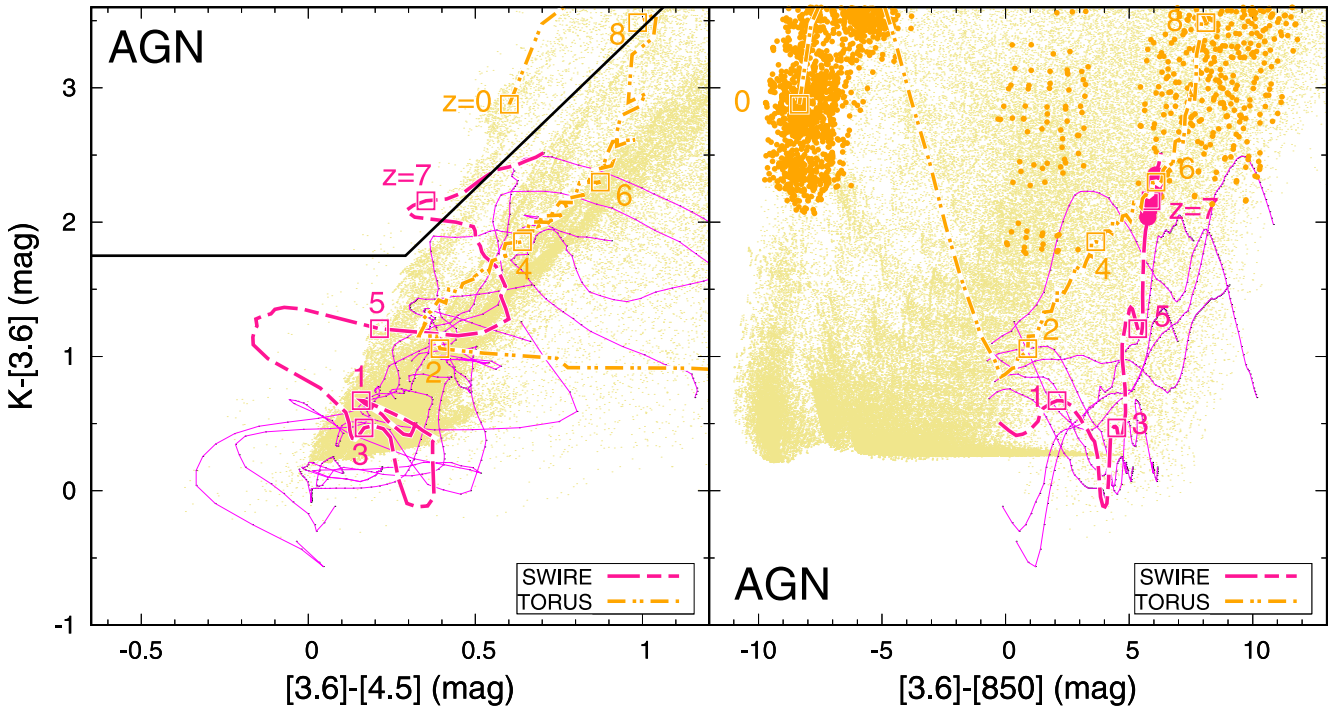

Figure 4. Same as Figure 3, but for the AGN templates from the SWIRE library (magenta thin curves; Polletta et al. 2007) and the theoretical TORUS models (yellow dots; Fritz et al. 2006; Feltre et al. 2012). For the TORUS template colors, we only show those at limited redshifts ($z = 0$, 1, 2, 3, 4, 5, 6, 7, and 8) for display purposes. The thick curves are characteristic examples: the SWIRE QSO2 template and one of the type 2 TORUS templates.

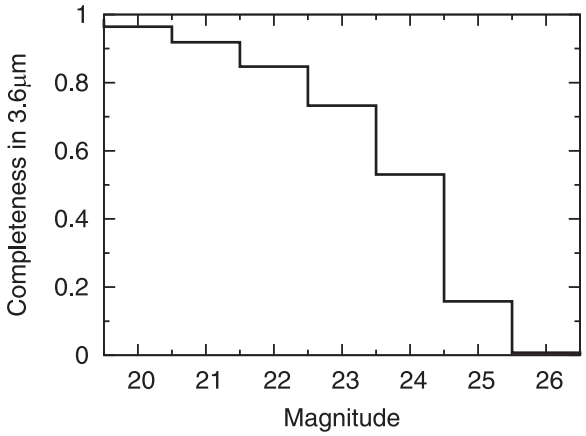

Figure 5. Completeness of source extraction in the [3.6]-band image. This is evaluated by extracting artificial objects in the same manner as the parent sample selection (see the text).

a possible spatial offset between the *HST* image and the [3.6]-band image, the latter of which has much coarser resolution. The measured magnitudes were corrected for Galactic extinction with $A_{F814W} = 0.03$, $A_g = 0.07$, $A_r = 0.05$, $A_i = 0.04$, $A_z = 0.03$, $A_y = 0.03$, $A_Y = 0.02$, $A_J = 0.02$, $A_H = 0.01$, and $A_{[5.8]} = A_{[8.0]} = 0$, which were estimated for the center of the COSMOS field based on Schlegel et al. (1998). For wavelengths longer than 10 μm and X-ray, we used the publicly available catalogs constructed by the individual survey teams (Section 2).

As shown in Figure 4, an additional criterion of [3.6]–[850] < -5 should remove DGs, DNLEs, and type 2 AGNs, except for objects with spectra similar to the $z \sim 0$ TORUS model. We practically adopted nondetection in all available FIR data whose depths were much shallower than those of the SPLASH [3.6] band (Table 1). The X-ray and radio data were also useful to remove AGNs. If the Lyα emission line is strong enough to boost the broadband flux, DNLEs may be detected in the optical bands.

No object in the color-selected sample was matched with any source in the X-ray and FIR catalogs. One object matched with a source in the VLA 3 GHz catalog (Smolčić et al. 2017), which was removed from our sample. We discarded 15 objects detected in some of the optical bands (shorter than *Y*) with a significance of more than 2σ. We further excluded an object because its [3.6]-band photometry was obviously affected by a nearby extended galaxy. The remaining six objects were recognized as BBG candidates at $5 \lesssim z \lesssim 8$. Their coordinates and photometry are shown in Table 2. Hereafter, their names, SPLASH_COSMOS_z6BBG_XX, are simplified as "BBG_XX." Their sky and color distributions[26] are shown in Figures 1 and 6, respectively. Figure 7 shows the multiband images of the six BBG candidates, where we select representative bands among many nondetection images.

At 0.4 μm $< \lambda <$ 1 μm, we also checked publicly available catalogs from the *HST*-COSMOS and HSC-SSP. Among the six candidates, only BBG_29 is in the HSC-SSP catalog (Aihara et al. 2019). Its *i*-band magnitude in the catalog is $\sim$27 mag, corresponding to S/N $\sim$ 5. By close inspection, we found that the catalog magnitude of BBG_29 was actually overestimated because of the locally enhanced background sky fluctuation. Flux measurements of the marginally detected objects are sensitive to photometric parameters such as aperture

[26] The *K*-band weight map released by the UltraVISTA team reveals homogeneous local sky variance in UVISTA UD stripes 2 and 3. Only BBG_30 among the six candidates lies at the edge of the *K*-band image, where the local sky variance is larger than 1.2× the average in the UD stripes. Even if we conservatively adopt a 0.2 mag shallower limiting magnitude in the *K* band than the representative (Table 1), all six candidates satisfy the *K*–[3.6] color criterion (Figure 6).

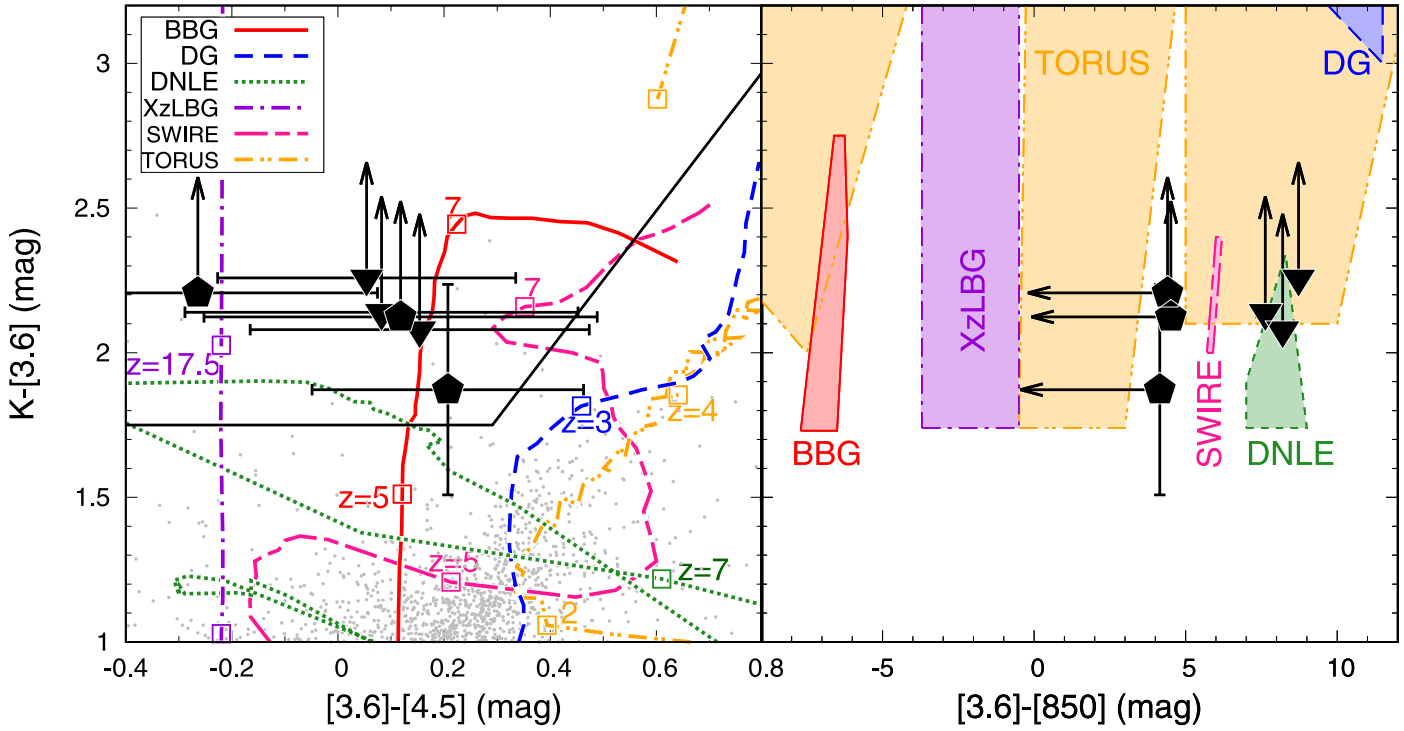

Figure 6. Color distributions of the BBG candidates with and without ALMA detections are shown with triangles and pentagons, respectively, in the K–[3.6] vs. [3.6]–[4.5] (left) and K–[3.6] vs. [3.6]–[850] (right) diagrams. Here we used the ALMA Band 7 data for the 850 μm photometry (Section 5). The arrows indicate 2σ limits for nondetections in K or ALMA Band 7. In the left panel, the characteristic template tracks are superposed by thick curves, which are the same as those in Figures 3 and 4. We also show K–[3.6] and [3.6]–[4.5] colors of all objects in the parent sample (gray dots). The BBG color selection boundary is shown by the black solid line. In the right panel, the shaded polygons correspond to the areas occupied by the Star+Nebular+Dust and AGN templates satisfying the BBG color criteria (Equations (1) and (2)).

size and the width of an annulus for estimation of the sky level. We again measured the flux of all six candidates in all HSC broad bands, adopting various combinations of aperture sizes (=1–2× PSF) and sky annuli (5″–21″). The resultant fluxes were very faint, typically with S/N < 2 for any candidate in any band. Exceptions were found for the i and z bands of BBG_22, as well as the i band of BBG_29, where the S/N reached as high as ∼3 by a few combinations of the aperture sizes and sky annuli. Even with the brightest measurements in the i and z bands (i band) for BBG_22 (BBG_29), our results based on the SED analysis remain unchanged (Section 6).

5. Follow-up ALMA Band 7 Observations

The *Herschel* and JCMT/SCUBA-2 data in the COSMOS field are the deepest among the existing wide-field FIR images and allow us to marginally distinguish BBGs from dusty contaminants such as DGs and DNLEs. For conclusive discrimination, however, the FIR limit had to be deepened. Therefore, we conducted ALMA follow-up observations for the BBG candidates.

The ALMA Band 7 observations (ID 2017.1.01259.S; PI: K. Mawatari) were performed in Cycle 5. We observed the six BBG candidates and an additional six filler objects. The observations were performed in 2018 April, May, August, September, and October under the antenna configurations of C43-2, C43-3, C43-4, and C43-5. The total on-source integration time was 38.8 minutes for each target. Four spectral windows (SPWs) with a total bandwidth of 7.5 GHz were set at central frequencies of 336.5, 338.4, 348.5, and 350.5 GHz. The corresponding wavelength coverages were $\lambda = 853$–863 and 883–893 μm. The spectral resolution was set to 15.6 MHz in the time division mode (TDM), which is enough to measure the continuum. The following QSOs were used for calibrations: J1058+0133, J0948+0022, J1037−2934, and J0854+2006 for atmospheric calibration; J1058+0133, J0948+0022, J0942−0759, J1037−2934, and J0854+2006 for water vapor radiometer (WVR) calibration; J1058+0133, J1037−2934, J0942−0759, and J0854+2006 for pointing calibration; J1058+0133, J1037−2934, and J0854+2006 for bandpass and flux calibration; and J0948+0022 for phase calibration. According to the ALMA proposer's guide, the flux calibration uncertainty is expected to be less than 10% in Band 7.

The data reduction and calibration were performed using the Common Astronomy Software Application (CASA) pipeline version 5.4.0. We collapsed all channels to produce a dust continuum image using the CASA task `CLEAN` with the natural weighting. The resulting synthesized beam size in FWHM was $0\farcs48 \times 0\farcs42$ with a position angle (PA) $\approx -78°$. We achieved a 1σ rms level of $\sim 30\,\mu$Jy beam^{-1} for all target objects. Photometry for the 12 targets was performed on the dust continuum images using the CASA task `imfit`, which fits the observed data within 2″ diameter apertures centered at the [3.6]-band detected positions with 2D Gaussian light profiles.

Three of the six BBG candidates (eight of the 12 targets in total) were detected in the continuum images. We hereafter focus on the BBG candidates, whose postage-stamp ALMA images are shown in Figure 7. Their ALMA Band 7 flux density measurements are summarized in Table 2. For the three BBG candidates not detected in ALMA Band 7, we obtained the flux density upper limits assuming point-like sources. The constraint on the FIR photometry became about 2 orders of magnitude deeper than the *Herschel* and SCUBA-2 data. Using

Table 2
Observed Properties of the BBG Candidates

Name	R.A. (deg)	Decl. (deg)	K (mag)	[3.6] (mag)	[4.5] (mag)	ALMA Band 7 (mag)
Sample without ALMA Detections						
SPLASH_COSMOS_z6BBG_09	149.680749	2.062202	25.61 ± 0.31	23.74 ± 0.19	23.54 ± 0.17	>19.60
SPLASH_COSMOS_z6BBG_22	150.071625	2.645838	>26.2	23.99 ± 0.23	24.25 ± 0.25	>19.59
SPLASH_COSMOS_z6BBG_29	149.724422	1.757402	>26.2	24.10 ± 0.27	23.99 ± 0.26	>19.59
Sample with ALMA Detections						
SPLASH_COSMOS_z6BBG_19	150.074593	2.045192	>26.2	23.94 ± 0.22	23.88 ± 0.18	15.21 ± 0.03
SPLASH_COSMOS_z6BBG_27	149.825170	2.084366	>26.2	24.09 ± 0.26	24.01 ± 0.26	16.46 ± 0.09
SPLASH_COSMOS_z6BBG_30	150.220922	2.607786	>26.2	24.11 ± 0.26	23.96 ± 0.19	15.91 ± 0.07

Notes. The 2σ limiting magnitudes are shown for the fainter objects, where we assume that they are point-like sources.

the ALMA Band 7 continuum flux density, we plotted the [3.6]–[850] colors of the six BBG candidates in the right panel of Figure 6. The colors of the three BBG candidates without any ALMA detection are hard to explain with the DG and DNLE models or SWIRE AGN templates. We therefore conclude that they are the most likely BBG candidates at $5 \lesssim z \lesssim 8$, although the contamination from dusty tori of type 2 AGNs or XzLBGs cannot be completely ruled out.

6. SED Fitting

6.1. Fitting Method

We performed SED fitting analyses of the multiband photometric data at wavelengths between 0.4 and 1000 μm (from HSC g to ALMA Band 7) for the six BBG candidates presented in Section 4. We mainly discuss the three candidates without ALMA detections in the following sections. Results for the other three candidates with ALMA detections are shown in Appendix B. The fitting code used in this study is our original SED analysis package (PANHIT) that is publicly available from our website.[27] We followed a χ^2 minimization algorithm for data including upper limits proposed by Sawicki (2012) but modified the formula slightly. Our definition of the χ^2 is

$$\chi^2 = \sum_i \left(\frac{f_{\mathrm{obs},i} - s f_{\mathrm{temp},i}}{\sigma_{\mathrm{obs},i}} \right)^2 - 2 \sum_j \times \ln \left[\frac{1}{\sqrt{2\pi}\,\sigma_{\mathrm{obs},j}} \int_{-\infty}^{f_{\mathrm{lim},j}} \exp\left\{ -\frac{1}{2} \left(\frac{f - s f_{\mathrm{temp},j}}{\sigma_{\mathrm{obs},j}} \right)^2 \right\} df \right], \quad (3)$$

where f_{obs}, σ_{obs}, and f_{temp} are the observed flux density, its uncertainty, and the template flux density, respectively. In Equation (3), the indices i and j in the summations of the first and second terms on the right-hand side correspond to the detection and nondetection bands, respectively. Here we regard the flux density brighter (fainter) than the 2σ limit as a detection (nondetection) for the bands at $\lambda < 10\ \mu$m. At longer wavelengths, the BBG candidates are not detected in all bands (Section 4.2), except for the three candidates in ALMA Band 7 (Section 5). Following treatment in Sawicki (2012), the upper limit of the integral in the nondetection band term, f_{lim}, is set to the 1σ limiting flux density. The scaling factor, s, is estimated analytically using only the detection bands:

$$s = \sum_i \frac{f_{\mathrm{obs},i} f_{\mathrm{temp},i}}{\sigma^2_{\mathrm{obs},i}} \Bigg/ \sum_i \frac{f^2_{\mathrm{temp},i}}{\sigma^2_{\mathrm{obs},i}}. \quad (4)$$

Three groups of templates were prepared for SED fitting. The fitting parameter ranges in each template group are summarized in Table 3. The first group, called the Galaxy group, consists of the Star+Nebular+Dust templates (Section 3.1) at $0 < z < 8$ with a wide variety of physical parameters. For the exponentially declining/rising SFH in the Star+Nebular+Dust models, we restricted the e-folding timescale to $\tau_{\mathrm{SFH}} \geqslant 30$ Myr. The lower limit of τ_{SFH} was determined to make it comparable to the freefall time of a spherically symmetric system virialized at $z \sim 20$ (Mo et al. 2010). The $\tau_{\mathrm{SFH}} = 30$ Myr is much longer than the gas cooling time for a halo with gas mass less than $10^{10}\ M_\odot$ at $z > 10$ (Mo et al. 2010). The second template group, called the AGN group, consists of AGN templates (Section 3.2). The empirical SWIRE AGN templates that are already reddened by dust are further reddened or dereddened by $-2 \leqslant A_V \leqslant +2$. We did not consider any dust reddening for the theoretical TORUS templates. The third template group, called the XzLBG group, is for possible XzLBG solutions. This third group consists of the Star+Nebular +Dust templates with a redshift range as high as $10 < z < 30$ and relatively simplified settings for the other model parameters (Table 3). We performed SED fitting separately with the above three template groups because we cannot know which template type is physically probable for each BBG candidate in advance.

For dust attenuation, while we mainly show the results with the Calzetti law (Calzetti et al. 2000) in the following sections, we also adopted the MW (Seaton 1979) and Small Magellanic Cloud (SMC; Prevot et al. 1984) laws. In our preliminary SED analyses, we occasionally obtained peculiar solutions with an almost zero SFR and extremely high dust attenuation. These solutions seem to be unlikely, and we define the forbidden region in the A_V–SFR plane as $A_V > \max(4 \times \mathrm{SFR}^{0.3}, 3.5$; see Appendix A for details).

We adopted a Monte Carlo (MC) technique to evaluate the reliability of the fitting solutions. We repeated the SED fitting procedures for randomly perturbed SEDs. The perturbation added to the observed flux density was realized by drawing a random number from a Gaussian distribution whose standard deviation is equal to the 1σ uncertainty in each band. The distribution of the best-fit solutions in these MC realizations defines the probability of the fitting solutions, as well as the confidence intervals around the solutions. To avoid confusion, we hereafter refer to the template yielding the least χ^2 in the fitting to the actual observed

[27] http://www.icrr.u-tokyo.ac.jp/~mawatari/PANHIT/PANHIT.html

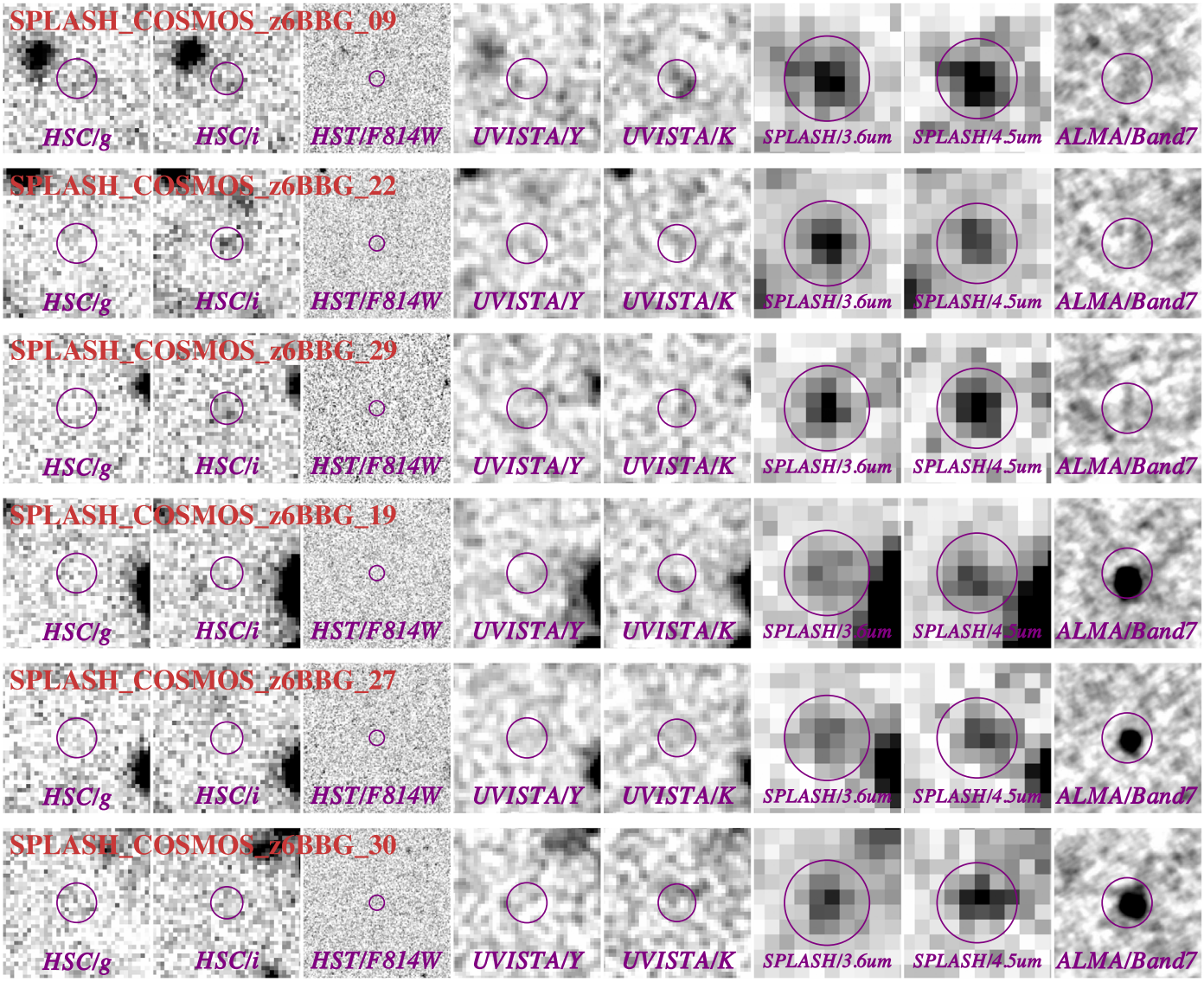

Figure 7. Postage-stamp images of the six BBG candidates in *g*, *i*, F814W, *Y*, *K*, [3.6], [4.5], and ALMA Band 7. The top three objects are not detected in ALMA Band 7, whereas the remaining three objects are detected. The panel size is always $6'' \times 6''$. The circle superposed on each panel shows the photometric aperture with diameters of $0\farcs6$ for F814W, $2''$ for ALMA Band 7, and $2\times$ the FWHM of the PSF for the other bands.

SED as the "best-fit" template and the one derived from each MC realization as the "MC-best" template.

6.2. BBG Candidates without ALMA Detection

Here we present the SED analyses for the three BBG candidates not detected in the ALMA observations. Because the ALMA Band 7 upper limits are deeper than the *Spitzer*/MIPS, *Herschel*, and JCMT/SCUBA-2 data, we used only the ALMA Band 7 data for the FIR range in the SED fitting. The resultant number of bands is 15: F814W, *g*, *r*, *i*, *z*, *y*, *Y*, *J*, *H*, K_s, [3.6], [4.5], [5.8], [8.0], and ALMA Band 7. In the following sections, we describe the SED fitting performed separately with the three template groups (Section 6.2.1) and that performed with composite templates of the galaxy and AGN models (Section 6.2.2).

6.2.1. Fitting with Either Galaxy or AGN or XzLBG Template Group

First, we perform the SED fitting with the Galaxy group templates (Table 3). As a result of 1000 MC runs, we found that the BBG models at $5 \lesssim z \lesssim 8$ are significantly favored for all three BBG candidates. Figure 8 shows the probability distributions of the five fitting parameters and the stellar mass of the 1000 MC-best templates. The MC-best models are massive ($M_* \sim 5 \times 10^{10}\ M_\odot$), dust-poor ($A_V < 0.2$), metal-enriched ($\sim Z_\odot$), and old (0.7–1 Gyr) galaxies at $5 \lesssim z \lesssim 8$. Their SFH is extremely bursty ($\tau_{\rm SFR} = 0.03$ Gyr), which leads to almost zero SFRs at the observed epoch.[28] The above SED properties are similar to those of local passive galaxies (e.g., Cox 2000; Phillipps 2005). We note that none of the 1000 MC realizations result in DG/DNLE solutions, except for BBG_9. In BBG_9, our MC realizations result in DG solutions on rare

[28] A small SFR is also expected from the observed photometry in the FIR and optical bands. We estimated the SFR upper limit from the ALMA Band 7 flux upper limit assuming a modified blackbody with a dust temperature of $T_d = 35$ K and a conversion factor from $L_{\rm IR}$ to SFR (Madau & Dickinson 2014). All three BBG candidates have SFR $\lesssim 10\ M_\odot\ {\rm yr}^{-1}$ (3σ). Almost the same constraint is obtained from the observed flux upper limit in the *Y* band that roughly corresponds to the rest-frame UV wavelength at the best-fit redshifts. The SFRs of the BBG candidates are an order smaller than those of the $z \sim 6$ star-forming galaxies on the main sequence (Speagle et al. 2014) with similar stellar masses ($\sim 5 \times 10^{10}\ M_\odot$).

Table 3
SED Fitting Parameters in the Three Template Groups

Group Name	Galaxy	AGN		XzLBG
Template Type[a]	Star+Nebular+Dust	SWIRE AGN	TORUS	Star+Nebular+Dust
Number of templates	2,818,260	7560	960,000	12,030
SFH	Exp-declining/rising ($\tau_{\rm SFH} = \pm$ 0.03, $\pm$0.06, $\pm$0.1, $\pm$0.3, $\pm$0.6, $\pm$1, and $\pm$10 Gyr), Constant SFR	⋯	⋯	Constant SFR
Metallicity (Z)	0.0001, 0.004, and 0.02	⋯	⋯	0.004
Age ($T_{\rm age}$) (Gyr)	0.001—age of the universe	⋯	⋯	0.001—age of the universe
Redshift[b]	0.1–7.9	0.1–7.9	0.1–7.9	10.1–29.9
A_V[c] (mag)	0–10	−2–+2	0	0–0.5

Notes.
[a] Three types of spectral templates are used: "Star+Nebular+Dust" is our galaxy spectral model including stellar, nebular, and dust emissions; "SWIRE AGN" denotes the empirical AGN templates from the SWIRE library (Polletta et al. 2007); and "TORUS" is the theoretical dust torus model (Fritz et al. 2006; Feltre et al. 2012).
[b] Redshift steps are $\Delta z = 0.2$.
[c] The dust attenuation step is $\Delta A_V = 0.2$, except for the XzLBG group, where $\Delta A_V = 0.1$ is adopted. For the Star+Nebular+Dust templates, dust attenuation A_V is limited to $A_V < \max(4 \times {\rm SFR}^{0.3}, 3.5)$ (see Appendix A).

occasions (1.7% occurrence rate).[29] We summarize the physical properties of the best-fit BBG models in Table 4, where the uncertainties are derived from the MC realizations excluding the DG solutions for BBG_9.

Next, we performed SED fitting with the AGN group templates (Table 3). We found that the $z \sim 0$ type 2 TORUS models are selected as the best-fit templates for all three candidates. From 300 MC iterations of the SED fitting, 68% confidence ranges on their redshifts are $z \lesssim 0.3$ for all three objects. Unfortunately, the type 2 TORUS models cannot be completely ruled out, even with our deep ALMA Band 7 constraints. This is because the type 2 TORUS dust emission is peaked at $\lambda \sim 40$ μm and becomes very faint in the longer FIR regime (Figure 2). In the MC-best TORUS models, the bolometric luminosity emitted by the central AGN, which is one of the model parameters (Fritz et al. 2006), is $L_{\rm bol} = (2.7^{+1.1}_{-0.7})$, $(3.0^{+14.1}_{-1.4})$, and $(3.3^{+3.2}_{-1.1}) \times 10^{41}$ erg s^{-1} for BBG_9, 22, and 29, respectively.

Finally, SED fitting with the XzLBG group templates results in the MC-best templates at $17 < z < 20$, $19 < z < 26$, and $19 < z < 27$ (68% confidence interval from 300 MC runs) for BBG_9, 22, and 29, respectively. All 300 MC realizations result in $A_V = 0$. Their stellar masses and SFRs are as large as $3 \times 10^9\,M_\odot \lesssim M_* \lesssim 3 \times 10^{10}\,M_\odot$ and $200\,M_\odot$ yr$^{-1} \lesssim$ SFR $\lesssim 2000\,M_\odot$ yr^{-1}, even at extremely high-z.

Figures 9–11 show the best-fit spectra from the three template groups for the three BBG candidates. All three types of template apparently agree well with the observed SEDs with the similar-fitting χ^2 values both in total and in each band. We confirmed that the above results do not significantly change if we change the dust attenuation law to the SMC or MW law.

As mentioned in Section 4.2, BBG_22 and BBG_29 are possibly detected with $>2\sigma$ in the HSC i or z bands. We also performed SED fitting for the brightest photometric measurements in the HSC bands (Section 4.2) with the same parameter setting as above. The best-fit χ^2 values are as large as 20–30. This is because no template can consistently reproduce all of the K–[3.6] and [3.6]–[4.5] colors, nondetection in ALMA Band 7, and detection in the i/z bands. We further attempted to fit the SEDs including the possible i/z detections with two stellar populations (see Hashimoto et al. 2018; Tamura et al. 2019). The best-fit solution was provided by a combination of an old passive model with $T_{\rm age} \approx 1$ Gyr and a young star-forming model with SFR $\lesssim 10\,M_\odot$ yr^{-1} at $5 \lesssim z \lesssim 5.5$. Because the best-fit stellar masses of the old passive components are very similar to those of the best-fit BBG models obtained above (Table 4), the following discussion about stellar mass density (SMD) and SFRD is not sensitive to whether or not the observed three galaxies are marginally detected in the HSC i or z bands.

6.2.2. Fitting with Composite Templates of the Star+Nebular+Dust and TORUS Models

In Section 6.2.1, we treated the galaxy and AGN templates separately because the connection between a galaxy and an AGN is not trivial and the number of the combinations is too large. In contrast, as every AGN is part of a galaxy, it is worthwhile to fit the observed SEDs with combined templates of Star+Nebular +Dust and AGN TORUS models (Fritz et al. 2006; Feltre et al. 2012). We generated 5,883,840 combined templates of the Star +Nebular+Dust and TORUS models at $0 < z < 8$. Although the Star+Nebular+Dust models we used here have the same parameter coverage as in the Galaxy group (Table 3), we reduced the parameter steps for $\tau_{\rm SFR}$, $T_{\rm age}$, and A_V. The TORUS models at each redshift are reduced from 24,000 to 10 representatives that are the same as those used in the code SED3FIT[30] (Berta et al. 2013). The TORUS spectra are scaled to the Star+Nebular+Dust models with a free parameter $L_{\rm bol}^{\rm TORUS}/M_*^{\rm Star+Nebular+Dust}$. Taking into account a relation between the BH mass and stellar mass of the host galaxy ($10^{-5} \lesssim M_{\rm BH}/M_* \lesssim 10^{-2}$; Reines & Volonteri 2015) and observations of the Eddington ratio (10^{-3} erg s$^{-1}\,M_\odot^{-1} < L_{\rm bol}/(1.25 \times 10^{38} \times M_{\rm BH}) < 10$ erg s$^{-1}\,M_\odot^{-1}$; Woo & Urry 2002), we set the parameter range as wide as 1.25×10^{30} erg s$^{-1}\,M_\odot^{-1} \leqslant L_{\rm bol}^{\rm TORUS}/M_*^{\rm Star+Nebular+Dust} \leqslant 1.25 \times 10^{37}$ erg s$^{-1}\,M_\odot^{-1}$ with a step of 1.0 in the common logarithmic scale.

[29] The DG solutions for BBG_9 have old stellar populations with $T_{\rm age} \sim 3$ Gyr, a short star formation timescale of $\tau_{\rm SFH} = 0.06$ Gyr, and dust attenuation of $A_V > 3$. In fact, these passive DG solutions are found around the boundary of the forbidden area of the SFR–A_V plane defined in Appendix A.

[30] http://steatreb.altervista.org/alterpages/sed3fit.html

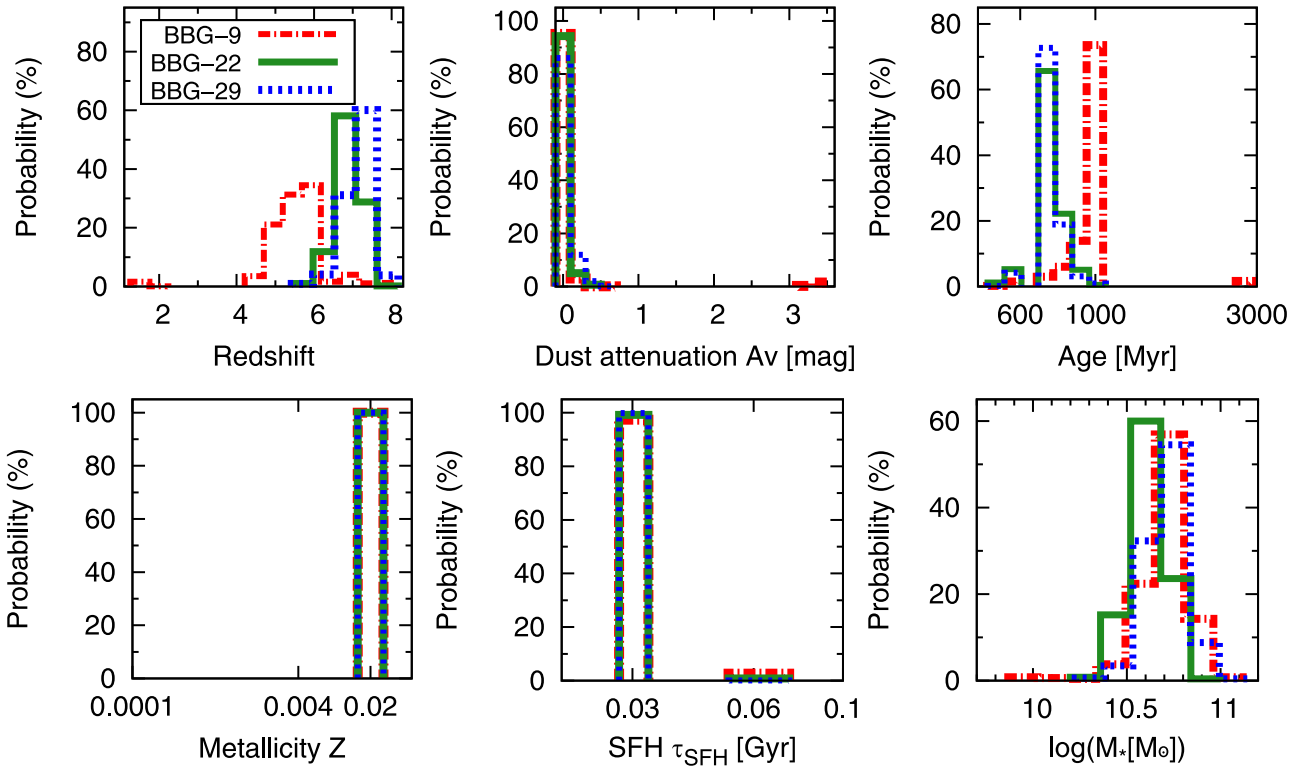

Figure 8. Probability distributions of physical quantities for the BBG candidates without ALMA detection. These are derived from 1000 MC realizations of the SED fitting with Galaxy group templates (see Table 3).

The resulting χ^2 values as a function of redshift are shown in Figure 12, where those from the original Star+Nebular+Dust or TORUS-only templates are also superposed. We found that the local χ^2 minima at high and low redshifts are achieved by templates dominated by the Star+Nebular+Dust or TORUS models, respectively. Templates equally contributed by the Star +Nebular+Dust and TORUS models do not show better fits than either of them for the observed SEDs. Therefore, we regarded the results in Section 6.2.1 as the fiducial ones in the following discussion.

7. Discussion

In this section, we focus on the three BBG candidates that are not detected in ALMA Band 7. First, we discuss the possible contamination to the BBG candidates (Section 7.1). Then, assuming all three candidates are real BBGs at $z \gtrsim 5$, we estimated their cosmic SMD and discussed the SFRD of their progenitors (Section 7.3).

7.1. Possibility of Contamination

7.1.1. AGNs at $z \sim 0$

Our SED fitting analyses reveal that heavily obscured AGN torus templates (type 2 TORUS) at $z \sim 0$ give as good fits as the BBG templates. In contrast, their SEDs are very unusual. Compared to the observed dusty AGN population (Polletta et al. 2007; Rigopoulou et al. 2009), the type 2 TORUS models show an order of magnitude larger flux density ratio of the rest-frame NIR ($\lambda \sim 2\,\mu$m) to FIR ($\lambda \sim 300\,\mu$m). At the Eddington accretion rate, the AGN bolometric luminosity is given by the Eddington luminosity, $L_{\rm Edd} = 1.25 \times 10^{38} \times M_{\rm BH}/M_\odot\,{\rm erg\,s^{-1}}$, where $M_{\rm BH}$ is the BH mass. Observationally, it is known that the AGN bolometric luminosity ranges over $0.001 \times L_{\rm Edd} < L_{\rm bol} < 10 \times L_{\rm Edd}$ (Woo & Urry 2002). Assuming this wide range of the Eddington ratio, we estimated the BH mass to be $240 \lesssim M_{\rm BH}/M_\odot \lesssim 2.4 \times 10^6$ from a typical bolometric luminosity of the best-fit TORUS models of $L_{\rm bol} \sim 3 \times 10^{41}\,{\rm erg\,s^{-1}}$ (Section 6.2.1). If the TORUS solution is the case for our BBG candidates, they may be the lowest-mass AGN BHs observed so far (Baldassare et al. 2015; Bentz & Katz 2015).

Furthermore, in the TORUS solution, emission from the host galaxy should be very faint at all wavelengths by definition (see Section 3.2). To constrain the properties of the host galaxies, we revisited SED fitting with the combined templates of the Star+Nebular+Dust and TORUS models (Section 6.2.2). We examined the combined templates whose χ^2 and redshift are similar to those of the best-fit $z \sim 0$ TORUS solutions. Their SEDs were almost dominated by the TORUS model templates

Table 4
Physical Properties of the Best-fit BBG Models

	BBG_9	BBG_22	BBG_29
χ^2	6.2	9.1	7.2
Redshift (z)	$5.5^{+0.6}_{-0.6}$	$6.9^{+0.3}_{-0.4}$	$7.1^{+0.5}_{-0.5}$
Dust attenuation (A_V) (mag)	$0.0^{+0.2}_{-0.0}$	$0.0^{+0.2}_{-0.0}$	$0.0^{+0.2}_{-0.0}$
Age ($T_{\rm age}$) (Gyr)	$1.02^{+0.0}_{-0.18}$	$0.72^{+0.14}_{-0.13}$	$0.72^{+0.12}_{-0.13}$
Metallicity (Z)	0.02[a]	0.02[a]	0.02[a]
Star formation timescale ($\tau_{\rm SFH}$) (Gyr)	$0.03^{+0.02}_{-0.00}$	$0.03^{+0.02}_{-0.00}$	$0.03^{+0.02}_{-0.00}$
Stellar mass (M_*) ($10^{10}\,M_\odot$)	$5.2^{+1.1}_{-1.3}$	$4.1^{+0.9}_{-0.8}$	$5.1^{+1.3}_{-1.0}$

Notes. The uncertainties are the 68% ranges of the distributions of the MC-best models in the SED fitting with Galaxy group templates. We removed 17 DGs at $z \lesssim 2$ among the 1000 MC-best models for BBG_9 to calculate the confidence ranges.
[a] All MC-best solutions fell in the same value.

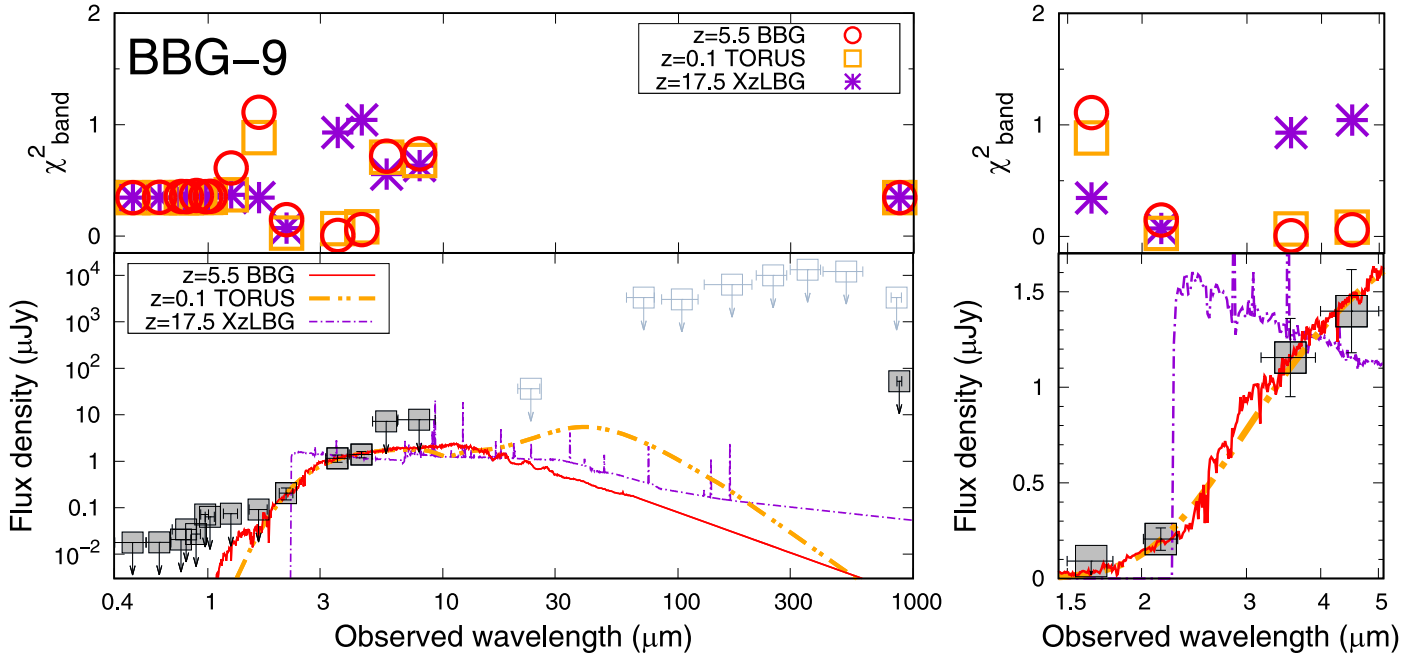

Figure 9. The observed SED of BBG_9 is shown in the bottom left panel, where filled (open) squares correspond to the observed photometry used (excluded) in the template fitting. For the nondetection bands, the 2σ limiting fluxes are set as upper limits, indicated by arrows. The best-fit spectra from the fittings with Galaxy, AGN, and XzLBG group templates are superposed. In the top left panel, χ^2 values of the individual bands for each template are shown. The right panels are the same as the left panels but with a zoom-in in the NIR wavelength range.

with a negligible contribution by the Star+Nebular+Dust templates, yielding a stellar mass of the host galaxies as $M_*^{\rm host} \lesssim 2 \times 10^6\,M_\odot$.

The estimated $M_{\rm BH}$ and $M_*^{\rm host}$ give a relatively high BH-to-total stellar mass ratio ranging from 10^{-4} to 1, of which only the lower boundary is consistent with an observed scaling relation (Reines & Volonteri 2015). Such an AGN with a very low mass BH hosted by a relatively low mass galaxy that contributes little to the whole SED ("low-mass naked" AGN) seems unlikely, while we reserve the complete rejection of the AGN solutions in the future.

7.1.2. LBGs at $z \gtrsim 17$

The XzLBGs at $z \gtrsim 17$ cannot be ruled out from the SED analyses. Especially for BBG_22, the observed blue [3.6]–[4.5] color prefers the XzLBG model rather than the BBG and TORUS models (Figure 10). The observed three BBG candidates had $[3.6] \sim 1\ \mu$Jy that corresponds to absolute rest-UV magnitudes of $M_{\rm UV} \sim -24.5$ mag at $z \sim 20$. Even with a very optimistic assumption that the UV luminosity function (UVLF) does not evolve beyond $z = 10$ (Bouwens et al. 2015), an expected number of the XzLBGs as bright as the observed objects is $\ll 1$ in the survey volume corresponding to $17 \leqslant z \leqslant 27$. Therefore, this possibility is also unlikely, although this case is highly interesting.

7.2. SMD of the z ∼ 6 BBGs

Compared to the DGs, AGNs, and XzLBGs mentioned in the previous sections, the BBG solutions at $z \sim 6$ may be physically acceptable for the three objects. The metallicity of the best-fit BBG model in the SED fitting is already the solar value in the $z \sim 6$ universe. This is consistent with the chemical evolution model (Asano et al. 2013) that predicts that matured galaxies with $T_{\rm age} \gtrsim 0.3$ Gyr and $M_* \gtrsim 10^{10}\,M_\odot$ can enrich their metallicity as high as the solar level (Tamura et al. 2019).

The passive nature of the $z \sim 6$ BBG model seems difficult to explain within the current theoretical framework of galaxy formation. This is because frequent galaxy interactions, gas supply into galaxies from the large-scale structure, and stellar feedback induce stochastic star formation (Trebitsch et al. 2017; Ceverino et al. 2018; Hopkins et al. 2018; Ma et al. 2018). We search for galaxies with similar stellar mass satisfying our BBG color criteria in an $\sim$1 Gpc^3 box of a semianalytic model (Makiya et al. 2016), resulting in no such counterpart at $z > 5$. In contrast, the prominent Balmer break is observationally confirmed in the $z = 9.1$ galaxy (Hashimoto et al. 2018), suggesting a passive phase lasting for $\sim$100 Myr or longer in galaxies even in the very early universe.

Assuming the three BBG candidates without ALMA detections to be passive galaxies at $4.8 \leqslant z \leqslant 7.8$ and correcting for the detection completeness (0.53 at $[3.6] \sim 24$ mag; Figure 5), we estimate the number density of the BBGs as $n_{\rm BBG} = (4.9^{+4.8}_{-2.7}) \times 10^{-7}$ Mpc^{-3} (comoving). Adopting the best-fit stellar mass and the uncertainties derived from the SED analysis, we obtained an SMD of $(2.4^{+2.3}_{-1.3}) \times 10^4\,M_\odot$ Mpc^{-3}.

Figure 13 (top panel) shows our SMD estimate as a function of redshift in conjunction with those from the literature for both passive galaxies (Muzzin et al. 2013; Straatman et al. 2014; Davidzon et al. 2017) and star-forming galaxies (Muzzin et al. 2013; Duncan et al. 2014; Grazian et al. 2015; Song et al. 2016; Davidzon et al. 2017; Bhatawdekar et al. 2019; Kikuchihara et al. 2019). The SMDs in the previous works, except for those in Straatman et al. (2014), are estimated by integrating the stellar mass functions (SMFs) down to $M_* = 10^8\,M_\odot$. In this work and Straatman et al. (2014), for passive galaxies at $z \sim 6$ and $\sim$4, respectively, however, the limited sample sizes prevented the authors from constructing SMFs. The estimated SMDs in Straatman et al. (2014) and this work are contributed only by massive galaxies down to the observational mass limits of $\sim 2 \times 10^{10}$ and $\sim 4 \times 10^{10}\,M_\odot$, respectively. This difference in the mass limits does not affect the SMDs for passive galaxies as much. This is because the SMFs for passive galaxies at $z \lesssim 4$ show a rapid decrease at $M_* \lesssim 3 \times 10^{10}\,M_\odot$ (Muzzin et al. 2013; Davidzon et al. 2017), and then the less massive galaxies

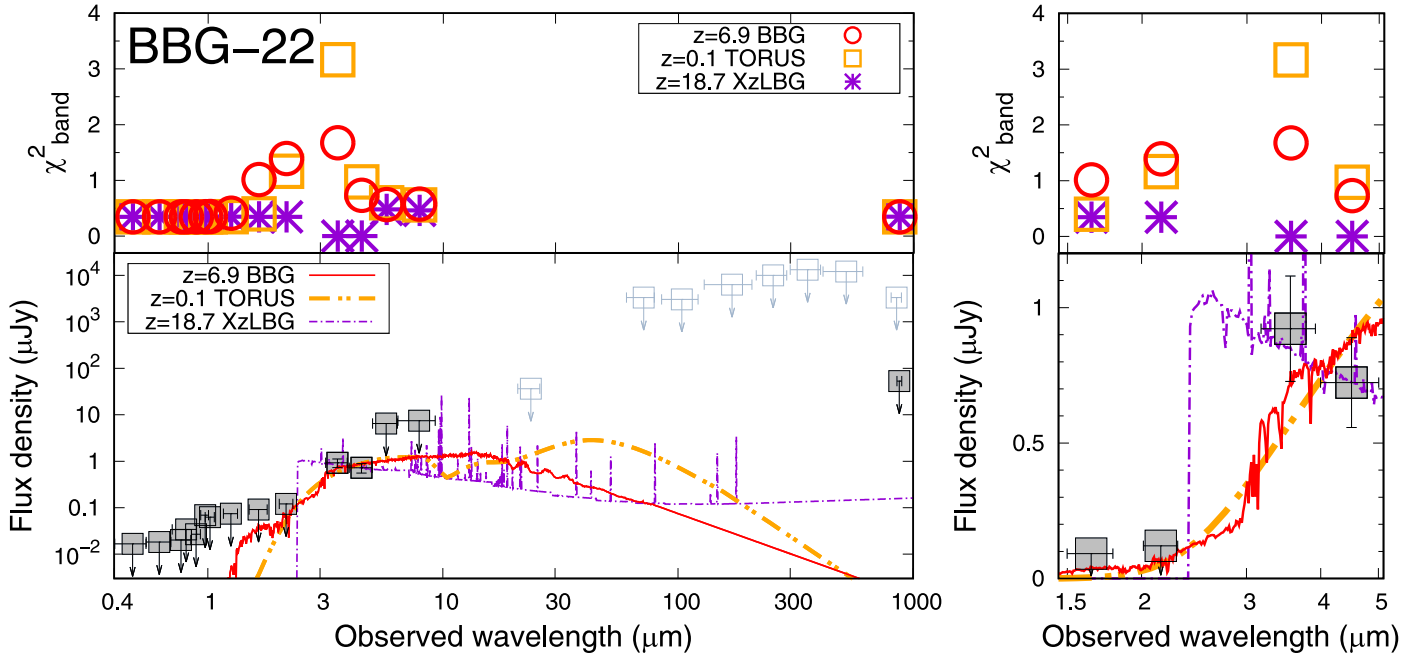

Figure 10. Same as Figure 9 but for BBG_22.

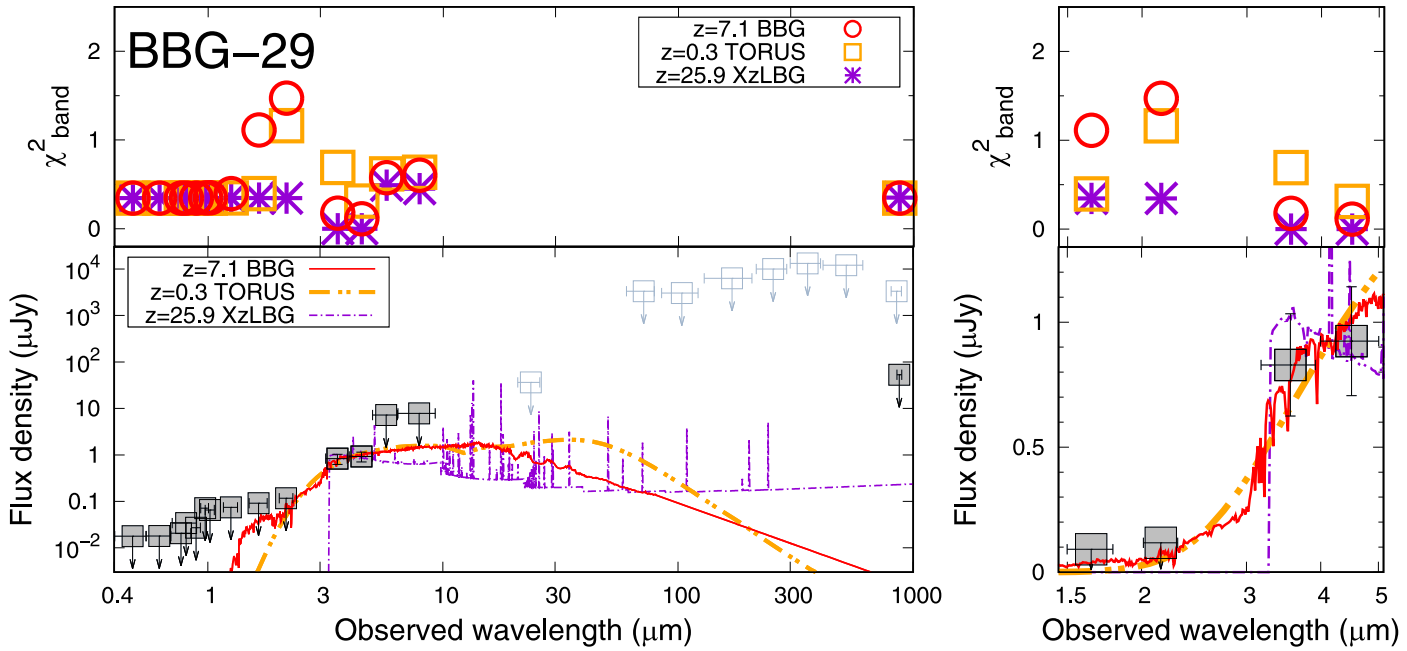

Figure 11. Same as Figure 9, but for BBG_29.

do not contribute to the SMDs. Our SMD at $z \sim 6$ is broadly consistent with the decreasing trend of passive galaxies from $z = 0$ to 4. The fraction contributed by the BBGs in the total SMD including star-forming galaxies at $z \sim 6$ is only ∼1%.

7.3. Cosmic Star Formation Activity at $z \gtrsim 14$

The small but nonzero number of BBGs suggests star formation activity by their progenitors at $z \gtrsim 10$, several hundred million yr or more before the observed epoch of $z \sim 6$. In the following section, we discuss the cosmic star formation activity by such progenitors, assuming that all three candidates are real BBGs.

The number density of the star-forming progenitors can be different from that of the BBGs because the progenitors are observable only during their star-forming phase ($T_{\rm SF}$), while the descendant BBGs are always observable once the Balmer break matures. Assuming the BBG observable time duration as $T_{\rm BBG} = T_{\rm age} - T_{\rm SF} - 0.2$ Gyr with $T_{\rm SF} = 2 \times \tau_{\rm SFH}$, where 0.2 Gyr is required to develop the Balmer break, we obtained the number density of the star-forming progenitors as $n_{\rm prog} = n_{\rm BBG} \times T_{\rm SF}/T_{\rm BBG} \approx 5.6 \times 10^{-8} (T_{\rm SF}/60\,{\rm Myr})$ Mpc^{-3} (comoving). We should note here that $T_{\rm SF}$ is not strongly constrained by the SED fitting. The observed Balmer break demands a sufficiently long $T_{\rm age}$. As a result, $T_{\rm SF}$ in the exponential SFH has to be short because of the limited cosmic time at $z \sim 6$. It is possible that an SFH having a certain star formation before the exponentially declining one provides a good fit to the BBGs' SED and allows a bit longer $T_{\rm SF}$

(but still limited by the short cosmic age). In this case, $n_{\rm prog}$ becomes larger than the above value accordingly.

We estimate the SFRD as

$$\rho_{\rm SFR} = \langle {\rm SFR} \rangle \times n_{\rm prog} = \sum_{i=1}^{3} {\rm SFR}_i^{\rm prog} \times \frac{1}{V_{\rm eff}} \times \frac{T_{{\rm SF},i}}{T_{{\rm BBG},i}}, \quad (5)$$

where $\langle {\rm SFR} \rangle$ is the average for the three objects, index i corresponds to each BBG, and $V_{\rm eff}$ is the effective survey volume at $4.8 < z < 7.8$ corrected for the detection incompleteness. Each progenitor's SFR (${\rm SFR}_i^{\rm prog}$) and star-forming duration ($T_{{\rm SF},i}$) are very sensitive to the SFH functional shape in the SED fitting. However, it can be approximated as

$$\rho_{\rm SFR} \approx \sum_{i=1}^{3} \frac{M_{*,i}^{\rm BBG}}{T_{{\rm SF},i}} \times \frac{1}{V_{\rm eff}} \times \frac{T_{{\rm SF},i}}{T_{{\rm BBG},i}} \approx \frac{\rho_*^{\rm BBG}}{\langle T_{\rm BBG} \rangle}, \quad (6)$$

where $\langle T_{\rm BBG} \rangle$ is an average for the three objects and $\rho_*^{\rm BBG}$ is the SMD of the $z \sim 6$ BBGs estimated in the previous section. This suggests that we can obtain the SFRD independent of the uncertain SFH and $T_{\rm SF}$. Therefore, the obtained SFRD may be as robust as the SMD because M_* and $T_{\rm BBG}$ are relatively well constrained by the observed IRAC flux density and [3.6]–[4.5] color (Balmer break strength).

Practically, we estimated the progenitors' SFRD adopting Equation (5) for the BBG models obtained from the SED analysis. Here we need to specify the timing to pick the SFR value and its redshift. We chose the model age the same as the star formation timescale ($T_{\rm age} = \tau_{\rm SFH}$), and this choice does not affect the obtained SFRD, as explained above. We made 10^6 combinations of three MC-best BBG models from the randomly selected 100 MC realizations for each object, from which we evaluated the confidence range on the SFRD. The progenitors' redshifts were simply averaged for each combination. The resultant 99.7% confidence range (3σ) on the progenitors' SFRD and redshift is shown in Figure 13 (bottom panel). Our estimate, $2.4 \times 10^{-5} \lesssim {\rm SFRD}/M_\odot\ {\rm yr}^{-1}\,{\rm Mpc}^{-3} \lesssim 1.2 \times 10^{-4}$ at $z \gtrsim 14$, should be regarded as a lower limit because not all star-forming galaxies at $z \gtrsim 14$ evolve into passive galaxies at $z \sim 6$. We also note that a similar estimate is obtained from Equation (6): $\rho_{\rm SFR} \approx (2.4 \times 10^4\ M_\odot\ {\rm Mpc}^{-3})/(0.56\ {\rm Gyr}) = 4.3 \times 10^{-5}\ M_\odot\ {\rm yr}^{-1}\,{\rm Mpc}^{-3}$, where $\langle T_{\rm BBG} \rangle = 0.56$ Gyr.

For comparison, we collected SFRD measurements at $z \lesssim 10$ from the literature (Oesch et al. 2013, 2014, 2018; Madau & Dickinson 2014; Finkelstein et al. 2015a; Bouwens et al. 2016; McLeod et al. 2016; Ishigaki et al. 2018; Bhatawdekar et al. 2019). Among these, the measurements at $4 \lesssim z \lesssim 10$ were converted from UV luminosity densities derived by integrating the UVLFs down to a certain luminosity or magnitude limit ($L_{\rm lim}$ or $M_{\rm lim}$). To correct for the different $M_{\rm lim}$ and conversion factors from UV luminosity densities to SFRDs adopted in previous works, we reintegrated their UVLFs down to $M_{\rm lim} = -17$ and multiplied the conversion factor of Madau & Dickinson (2014). The measurements of Madau & Dickinson (2014) were actually not reestimated because their adopted $L_{\rm lim} = 0.03L^*$, where L^* is the characteristic luminosity of the UVLF, corresponds to $M_{\rm lim} = -17$ mag at $z \sim 3$ (Reddy & Steidel 2009). All of the literature measurements are also corrected for the IMF and the cosmological parameters to match with those adopted in this work.

The SFRDs from the previous works after the above corrections are shown in Figure 13. In addition to the direct measurements at $z \lesssim 10$, we also put an SFRD estimate at $z \sim 17$ (yellow shaded region in Figure 13) based on the UV luminosity density of Madau (2018) using an SFR conversion factor (Madau & Dickinson 2014) corrected for the IMF. The UV luminosity density of Madau (2018) was estimated to reproduce a tentative detection by the EDGES collaboration of the global 21 cm absorption trough imprinted in the cosmic microwave background (CMB) spectrum (Bowman et al. 2018) under the assumption that the 21 cm signal is activated by extremely metal-poor stellar systems.

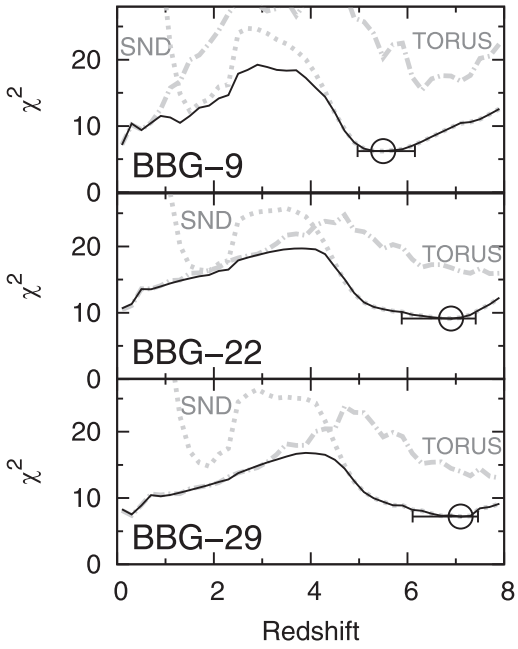

Figure 12. The SED fitting χ^2 as a function of redshift for the three BBG candidates without ALMA detection. Dotted, dotted–dashed, and solid lines correspond to the χ^2 distributions in the fitting with the Star+Nebular+Dust, TORUS, and their composite templates (see the text), respectively. The circles with error bars show the least χ^2 point and the range of $\Delta\chi^2 \leqslant 1$ in the fitting with the Star+Nebular+Dust and TORUS composite templates.

We now revisit the frequently debated topic of SFRD evolution at $z \gtrsim 8$. In Figure 13, four possible evolutionary trends are also shown. Two support a smooth evolution from $z \sim 5$ to 10: the functional fit to the measurements of Madau & Dickinson (2014) that is proportional to $(1+z)^{-2.9}$ at $z > 3$ and a bit steeper power-law function with the slope $\alpha = -4.3$ proposed by Finkelstein et al. (2015a). The others support a rapid SFRD decline at $z \gtrsim 8$: a power-law function with the slope $\alpha = -10.9$ (Oesch et al. 2014) and an expected evolution assuming no redshift dependence on the relation among the halo mass, SFR, and dark matter accretion rate (Harikane et al. 2018). Our SFRD estimate at $z \gtrsim 14$ seems consistent with the smooth SFRD evolution. If our SFRD is a lower limit, as discussed above, it is also consistent with the $z \sim 17$ estimate based on the EDGES detection of the 21 cm absorption signal (Bowman et al. 2018; Madau 2018) that is on the extrapolation of the Madau & Dickinson (2014) best-fit function. In contrast, the rapid decrease in the SFRD may not be consistent with our estimate. Because the rapid decline can be interpreted by the number density evolution of dark matter halos (Harikane et al. 2018; Oesch et al. 2018), our relatively high SFRD may indicate a higher star formation efficiency in the halos at $z \gtrsim 10$.

Individual progenitors of the BBGs should have produced their stellar mass of $\sim 5 \times 10^{10}\ M_\odot$ by $z \sim 14$. The number density of the star-forming progenitors, $n_{\rm prog} \approx 5.6 \times 10^{-8}\,{\rm Mpc}^{-3}$, implies their halo mass to be $\sim 10^{11}\ M_\odot$ ($\sim 10^{12}$) at $z \sim 17$ ($z \sim 11$; Mo & White 2002). Their stellar-to-halo mass ratios (SHMRs) are expected to be ~ 0.5 (~ 0.05) at $z \sim 17$ ($z \sim 11$). These are much

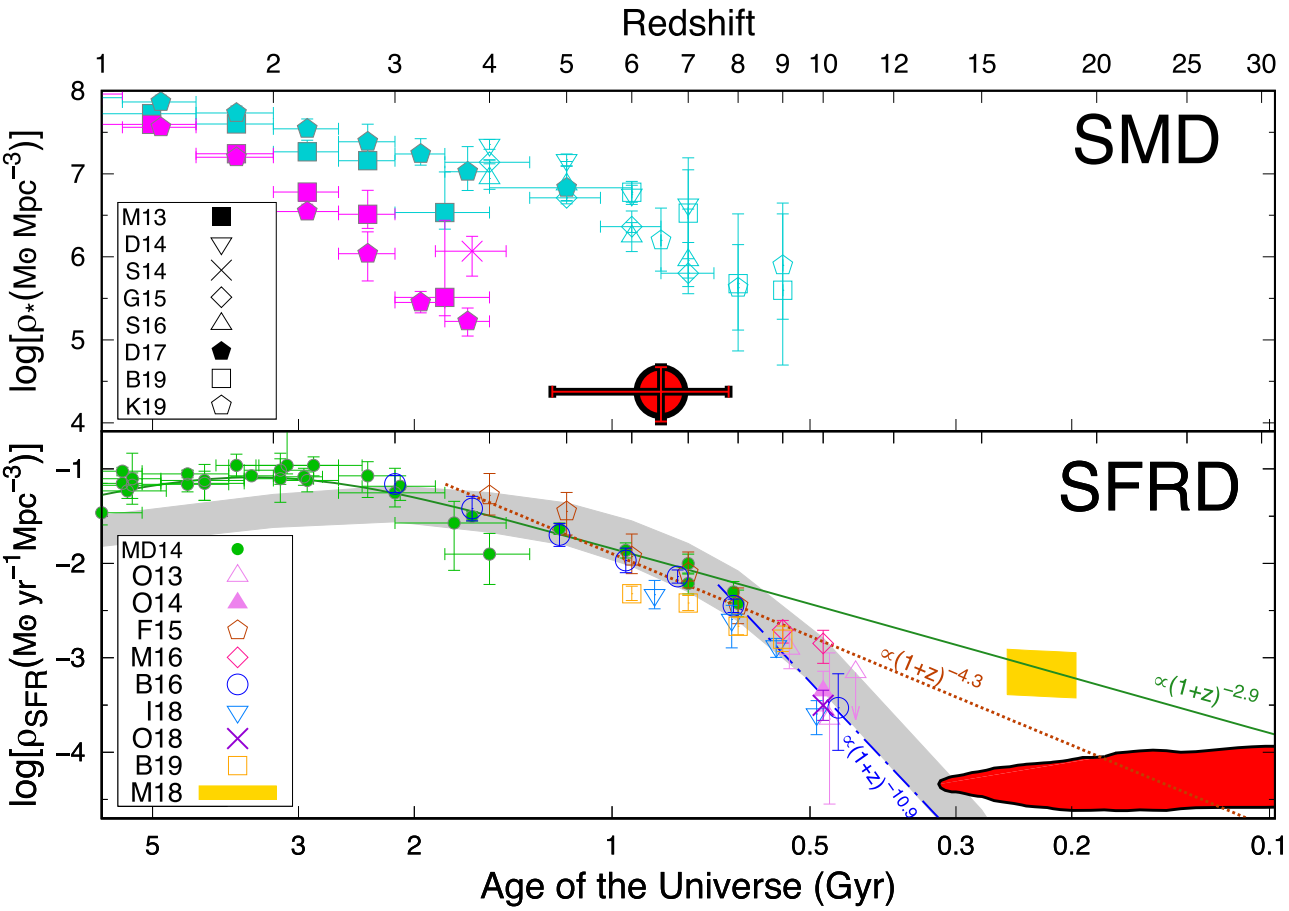

Figure 13. Evolution of the SMD (top) and SFRD (bottom) along the cosmic history (see top axis for the corresponding redshift). For these plots, we assumed all three BBG candidates without ALMA detection to be real passive galaxies at $z \sim 6$. In the top panel, the SMD of our BBG sample at $z \sim 6$ (red circle) is shown in conjunction with those of star-forming (cyan symbols) and passive (magenta symbols) galaxies at lower redshifts from the literature (M13: Muzzin et al. 2013; D14: Duncan et al. 2014; S14: Straatman et al. 2014; G15: Grazian et al. 2015; S16: Song et al. 2016; D17: Davidzon et al. 2017; B19: Bhatawdekar et al. 2019; K19: Kikuchihara et al. 2019). The vertical error bar associated with our BBG data corresponds to a 1σ uncertainty propagated from the Poisson error (Gehrels 1986) for the BBG number and the SED fitting uncertainty for the stellar mass. The horizontal error bar shows the redshift range expected from our BBG color selection. In the bottom panel, the red shaded region corresponds to the SFRD expected from the progenitors of the $z \sim 6$ BBGs at a 99.7% confidence level (3σ). The SFRD measurements at $z \lesssim 10$ are collected from the literature (MD14: Madau & Dickinson 2014; O13: Oesch et al. 2013; O14: Oesch et al. 2014; F15: Finkelstein et al. 2015a; M16: McLeod et al. 2016; B16: Bouwens et al. 2016; I18: Ishigaki et al. 2018; O18: Oesch et al. 2018; B19: Bhatawdekar et al. 2019). All of them at $4 \lesssim z \lesssim 10$ are estimated by integrating the UVLFs down to $M_{\rm UV} = -17$ mag. The SFRD estimated at $z \sim 17$ from an observed global 21 cm absorption trough (M18: Madau 2018; Bowman et al. 2018) is also shown in yellow. The functional fit to the MD14 data, which is proportional to $(1+z)^{-2.9}$ at high-z (Madau & Dickinson 2014), is superposed by the solid line. Two other power-law functions supporting an accelerated evolution at $z \gtrsim 8$ ($\rho_{\rm SFR} \propto (1+z)^{-10.9}$; Oesch et al. 2014) and a smooth evolution from lower redshift ($\rho_{\rm SFR} \propto (1+z)^{-4.3}$; Finkelstein et al. 2015a) are shown by dotted–dashed and dotted lines, respectively. The SFRD derived assuming a universal relation among the halo mass, SFR, and dark matter accretion rate (Harikane et al. 2018) is also superposed by the gray shade in its 1σ uncertainty. All of the SMD and SFRD measurements from the literature are corrected for the stellar IMF and the cosmological model to match those in this work.

larger than the SHMRs measured at lower redshift (e.g., Leauthaud et al. 2012; Behroozi et al. 2013). Our measurement is hard to explain if we linearly extrapolate a redshift evolution of SHMRs (Finkelstein et al. 2015b; Harikane et al. 2016) up to $z \sim 20$. The very high SHMRs again suggest an unexpectedly high star formation efficiency and/or low feedback efficiency in the BBG progenitor halos at the pre-reionization epoch. This problem should be resolved by theoretical works in the future.

8. Conclusion

In this study, we searched for passively evolving galaxies whose SEDs are characterized by the prominent Balmer break. The effective survey area is 0.41 deg^2 in the COSMOS field. Using the rich imaging data set available in the entire survey field, we photometrically identified six candidate BBGs. We performed follow-up observations with ALMA Band 7 for these BBG candidates. Three of the six candidate BBGs were detected in dust continuum emission. The remaining three candidates not detected with ALMA are promising BBG candidates. Through comprehensive SED analyses with a large template set of galaxy and AGN models, we obtained the following results and implications.

1. The three BBG candidates not detected with ALMA can be considered as the most likely BBGs at $z \sim 6$. The best-fit galaxy models for their SEDs have the following properties: $5 < z < 8$, $M_* \sim 5 \times 10^{10}\,M_\odot$, in the inactive star formation phase for $\gtrsim$0.7 Gyr, no dust attenuation/emission, and metal-enriched as a solar level.
2. The cosmic SMD estimated from the three most likely BBG candidates at $5 \lesssim z \lesssim 8$ is $\rho_* = (2.4^{+2.3}_{-1.3}) \times 10^4\,M_\odot$ Mpc^{-3}. This is consistent with the decreasing trend observed at $z < 4$.
3. The onset of star formation in the most likely BBG candidates should be at $z \gtrsim 14$. The cosmic SFRD contributed by the progenitors is expected to be

$2.4 \times 10^{-5} \lesssim \rho_{\rm SFR}/M_{\odot}\ {\rm yr}^{-1}\,{\rm Mpc}^{-3} \lesssim 1.2 \times 10^{-4}$ with 99.7% confidence (3σ). This SFRD estimate is less sensitive to SFHs assumed in the SED fitting analyses. The SFRD contributed by the progenitors of the BBGs is a lower limit of the total SFRD owed by all populations of galaxies at $z \gtrsim 14$. Our estimate supports a smooth evolution of SFRDs from $z \sim 5$ to beyond $z \sim 10$ rather than an accelerated evolution at $z \gtrsim 8$.

4. In the most likely BBG sample, however, there is still possible contamination from type 2 AGNs at $z \sim 0$ with very low mass ($240\,M_{\odot} \lesssim M_{\rm BH} \lesssim 2.4 \times 10^{6}\,M_{\odot}$) BHs hosted by relatively low mass galaxies ($M_{*}^{\rm host} \lesssim 2 \times 10^{6}\,M_{\odot}$) that contribute little to the whole SED. Such low-mass naked type 2 AGNs seem to be unlikely but very interesting, and follow-up observations with future deeper NIR or MIR instruments are needed.

While the above results are based on the best efforts using the highest-quality imaging data currently available, direct evidence of the BBG, i.e., spectroscopic confirmation of the Balmer break by the coming *James Webb Space Telescope* (*JWST*; Gardner et al. 2006), is needed. If our BBG sample is really at $z \gtrsim 5$, it is time to construct a new formation path for massive galaxies in the very early universe.

K.M. and A.K.I. acknowledge financial support from the Japan Society for the Promotion of Science (JSPS) through KAKENHI grant Nos. 26287034 and 17H01114, and grant No. 2016-01. T.H. was supported by Leading Initiative for Excellent Young Researchers, MEXT, Japan. Y.T. is supported by JSPS through KAKENHI grant No. 16H02166. We thank M. Sawicki for discussions regarding the SED fit algorithm, M. Akiyama for discussions regarding the AGN solutions, A. Goulding for discussions in the HSC data analysis, N. Scoville for interpretation of the SED fit results, and C. H. Lee for the English corrections. We also thank I. Smail and C. C. Chen for letting us know about the detections of the previously reported BBG candidate (Mawatari et al. 2016) by SCUBA-2 and ALMA. We would like to thank Editage (www.editage.com) for English language editing. We appreciate the observatories where the data used in this work were taken. The *Spitzer Space Telescope* is operated by the Jet Propulsion Laboratory, California Institute of Technology, under a contract with NASA. The UltraVISTA survey is based on data products from observations made with the ESO Telescopes at the La Silla Paranal Observatory under ESO program ID 179.A-2005 and on data products produced by TERAPIX and the Cambridge Astronomy Survey Unit on behalf of the UltraVISTA consortium. This paper makes use of the following ALMA data: ADS/JAO.ALMA #2017.1.01259.S. ALMA is a partnership of the ESO (representing its member states), NSF (USA), and NINS (Japan), together with the NRC (Canada), MOST and ASIAA (Taiwan), and KASI (Republic of Korea), in cooperation with the Republic of Chile. The Joint ALMA Observatory is operated by the ESO, AUI/NRAO, and NAOJ. The *HST* data used in this work were obtained through the data archive at the Space Telescope Science Institute, which is operated by the Association of Universities for Research in Astronomy, Inc., under NASA contract NAS 5-26555. The Hyper Suprime-Cam (HSC) collaboration includes the astronomical communities of Japan and Taiwan and Princeton University. The HSC instrumentation and software were developed by the National Astronomical Observatory of Japan (NAOJ), the Kavli Institute for the Physics and Mathematics of the Universe (Kavli IPMU), the University of Tokyo, the High Energy Accelerator Research Organization (KEK), the Academia Sinica Institute for Astronomy and Astrophysics in Taiwan (ASIAA), and Princeton University. Funding was contributed by the FIRST program from the Japanese Cabinet Office, the Ministry of Education, Culture, Sports, Science and Technology (MEXT), the Japan Society for the Promotion of Science (JSPS), the Japan Science and Technology Agency (JST), the Toray Science Foundation, NAOJ, Kavli IPMU, KEK, ASIAA, and Princeton University. This paper used software developed for the Large Synoptic Survey Telescope. We thank the LSST Project for making their code available as free software at http://dm.lsst.org. The Pan-STARRS1 Surveys (PS1) have been made possible through contributions of the Institute for Astronomy, the University of Hawaii, the Pan-STARRS Project Office, the Max Planck Society and its participating institutes, the Max Planck Institute for Astronomy, Heidelberg, and the Max Planck Institute for Extraterrestrial Physics, Garching, the Johns Hopkins University, Durham University, the University of Edinburgh, Queen's University Belfast, the Harvard-Smithsonian Center for Astrophysics, the Las Cumbres Observatory Global Telescope Network Incorporated, the National Central University of Taiwan, the Space Telescope Science Institute, the National Aeronautics and Space Administration under grant No. NNX08AR22G issued through the Planetary Science Division of the NASA Science Mission Directorate, the National Science Foundation under grant No. AST-1238877, the University of Maryland, Eotvos Lorand University (ELTE), and the Los Alamos National Laboratory. The HSC-SSP data were collected at the Subaru Telescope and retrieved from the HSC data archive system, which is operated by the Subaru Telescope and Astronomy Data Center at the National Astronomical Observatory of Japan. *Herschel* is an ESA space observatory with science instruments provided by European-led Principal Investigator consortia and with important participation from NASA. The SCUBA-2 is on the James Clerk Maxwell Telescope, which is operated by the East Asian Observatory on behalf of the National Astronomical Observatory of Japan, Academia Sinica Institute of Astronomy and Astrophysics, the Korea Astronomy and Space Science Institute, the National Astronomical Observatories of China, and the Chinese Academy of Sciences (grant No. XDB09000000), with additional funding support from the Science and Technology Facilities Council of the United Kingdom and participating universities in the United Kingdom and Canada. The VLA is a part of the National Radio Astronomy Observatory, which is a facility of the National Science Foundation operated under cooperative agreement by Associated Universities, Inc. The *XMM-Newton* satellite is an ESA science mission with instruments and contributions directly funded by the ESA Member States and NASA. The scientific results reported in this article are based in part on observations made by the *Chandra X-ray Observatory*.

Facilities: *Spitzer*(IPAC), VISTA(ESO), Subaru(NAOJ), *HST* (STIS), *Herschel*(ESA), JCMT(EAO), VLA(NRAO), *XMM-Newton*(ESA), *Chandra*(NASA).

Software: SExtractor (Bertin & Arnouts 1996), IRAF (Tody 1986, 1993), PANHIT (http://www.icrr.u-tokyo.ac.jp/~mawatari/PANHIT/PANHIT.html).

Appendix A
Forbidden Region in A_V versus SFR Parameter Space

There is a good correlation between A_V and SFR observed so far (Sullivan et al. 2001; Garn et al. 2010; Garn & Best 2010;

Price et al. 2014). We compiled galaxies in the literature to examine their distribution in the SFR–A_V plane. For the Sloan Digital Sky Survey (SDSS) DR7 sample (Abazajian et al. 2009), we used ∼100,000 galaxies for which the Hα and Hβ emission line fluxes are available in the MPA-JHU catalog.[31] The SFR is estimated from the Hα line flux (Brinchmann et al. 2004). The A_V is evaluated from the Hα/Hβ flux ratio (Chen et al. 2010) followed by a conversion from nebular to stellar attenuation (×0.44; Calzetti et al. 2000). We confirmed a correlation between the A_V and SFR for the local galaxies (Figure 14).

We also investigated *Herschel*-detected samples comprising 29 submillimeter galaxies (SMGs) at $z > 1$ (Magnelli et al. 2012; Rowlands et al. 2014), 42 galaxies at $z < 0.5$ with early-type morphology (Rowlands et al. 2012), and 19 galaxies at $z < 0.5$ with small SFR and late-type morphology (Rowlands et al. 2012). They are rare populations of galaxies and supplementary to local typical galaxies from the SDSS sample. Rowlands et al. (2012, 2014) released the physical quantities of the *Herschel*-detected DGs estimated with the SED fitting code MAGPHYS (da Cunha et al. 2008), from which we extracted the values of the SFR and dust optical depth for stellar emission. There are two types of dust optical depths, one of stellar birth clouds (BCs) and the other of the interstellar medium (ISM), because MAGPHYS allows different amounts of attenuation in the BCs and ISM (da Cunha et al. 2008). We show both attenuation values in the BCs and ISM ($A_V^{\rm BC}$ and $A_V^{\rm ISM}$) for *Herschel*-detected DGs in Figure 14. The $A_V^{\rm BC}$ is always larger than $A_V^{\rm ISM}$ (Charlot & Fall 2000; da Cunha et al. 2008). The dust attenuation for stellar emission averaged over the whole galaxy is expected to be between $A_V^{\rm BC}$ and $A_V^{\rm ISM}$, depending on the luminosity ratio of young stars in the BC and old stars in the ISM (da Cunha et al. 2008).

We can physically interpret the correlation between A_V and SFR (Figure 14) via a well-established correlation between gas column density and surface SFR density (Schmidt–Kennicutt law; Schmidt 1959; Kennicutt 1998). Given a dust-to-gas ratio from an MW measurement ($A_V/N_{\rm H} = 5.3 \times 10^{-22}$ cm^2 mag atms^{-1}; Bohlin et al. 1978; Rachford et al. 2009; Draine 2011), the Schmidt–Kennicutt law leads to a correlation between surface SFR density and dust attenuation. We convert the surface SFR density to SFR by combining a size–mass relation (Shen et al. 2003) and a mass–SFR relation (main sequence of star-forming galaxies; Speagle et al. 2014). In Figure 14, we show the expected relation, $A_V = 0.9 \times {\rm SFR}^{0.3}$, with the dotted–dashed curve, which well reproduces the measurements for the SDSS galaxies.

Based on the above consideration, we conservatively define a forbidden region in the A_V–SFR plane for this work as $A_V > \max(4 \times {\rm SFR}^{0.3}, 3.5$; shaded area in Figure 14). There are three *Herschel*-detected galaxies whose $A_V^{\rm BC}$ and SFR are inside the forbidden region. We checked the fractions of dust attenuated energy by the BCs and ISM (f_μ in Rowlands et al. 2012), confirming that dust attenuation in the three galaxies largely occurs in the ISM. Then, the dust attenuation for the whole stellar emission from the individual galaxies should be similar to the $A_V^{\rm ISM}$, which is far from the forbidden region.

[31] https://wwwmpa.mpa-garching.mpg.de/SDSS/DR7/

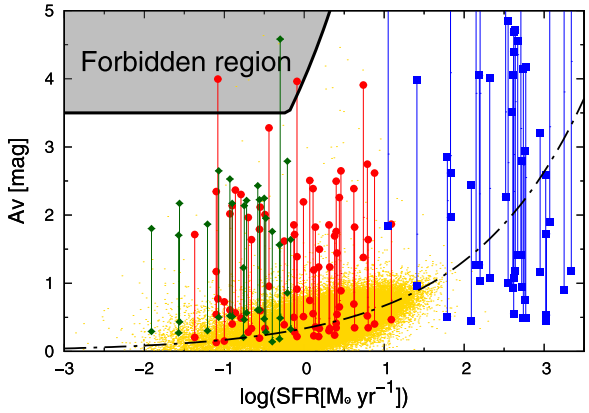

Figure 14. Forbidden region in SFR vs. A_V parameter space in the SED fitting (gray shaded area). The dotted–dashed curve corresponds to the relation expected from the Kennicutt–Schmidt law (Kennicutt 1998), gas-to-dust ratio in the MW (Bohlin et al. 1978; Rachford et al. 2009; Draine 2011), and empirical relations of size-to-mass (Shen et al. 2003) and mass-to-SFR (Speagle et al. 2014) for the main-sequence galaxies at $z \sim 0$. The yellow dots show the measurements for the SDSS galaxies (Abazajian et al. 2009; Chen et al. 2010). Blue squares, red circles, and green diamonds are the *Herschel*-detected sample of SMGs at $z > 1$ (Magnelli et al. 2012; Rowlands et al. 2014), DGs with early-type morphology (Rowlands et al. 2012), and dusty passive galaxies with late-type morphology (Rowlands et al. 2012), respectively. For every *Herschel*-detected galaxy, we show two kinds of dust attenuation, $A_V^{\rm BC}$ and $A_V^{\rm ISM}$, which are connected with vertical lines. Dust attenuation for stellar emission from a whole individual galaxy should be between $A_V^{\rm BC}$ and $A_V^{\rm ISM}$.

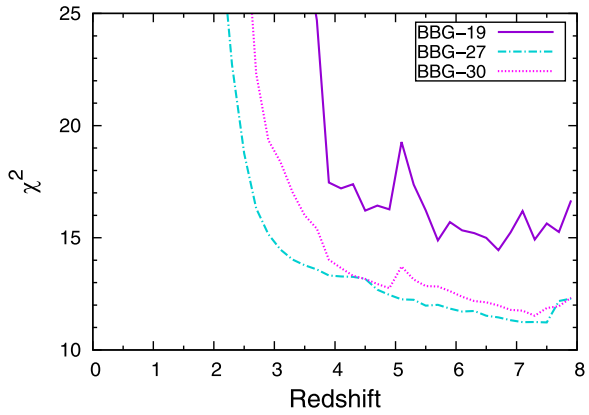

Figure 15. The SED fitting χ^2 as a function of redshift for the three BBG candidates with ALMA detection.

Appendix B
BBG Candidates with ALMA Detection

For the three BBG candidates detected in the ALMA observations, we performed SED fitting in the same manner as in Section 6.1. In the FIR regime, not only the ALMA Band 7 flux density but also the upper limits in other instruments were useful to constrain the overall IR SED shape. Therefore, we used all bands between 0.4 and 1000 μm, except for SCUBA-2, whose wavelength is almost the same as that of ALMA Band 7.

We found that DG and DNLE templates in the Galaxy group are significantly preferred to the AGN group templates for all three objects. Their physical properties are not constrained very much, except for dust attenuation (and the IR luminosity as its derivative). This is due to the large redshift uncertainties. The χ^2 values are roughly constant at $z \gtrsim 4$, as shown in Figure 15. In contrast, 300 MC runs result in relatively narrow ranges

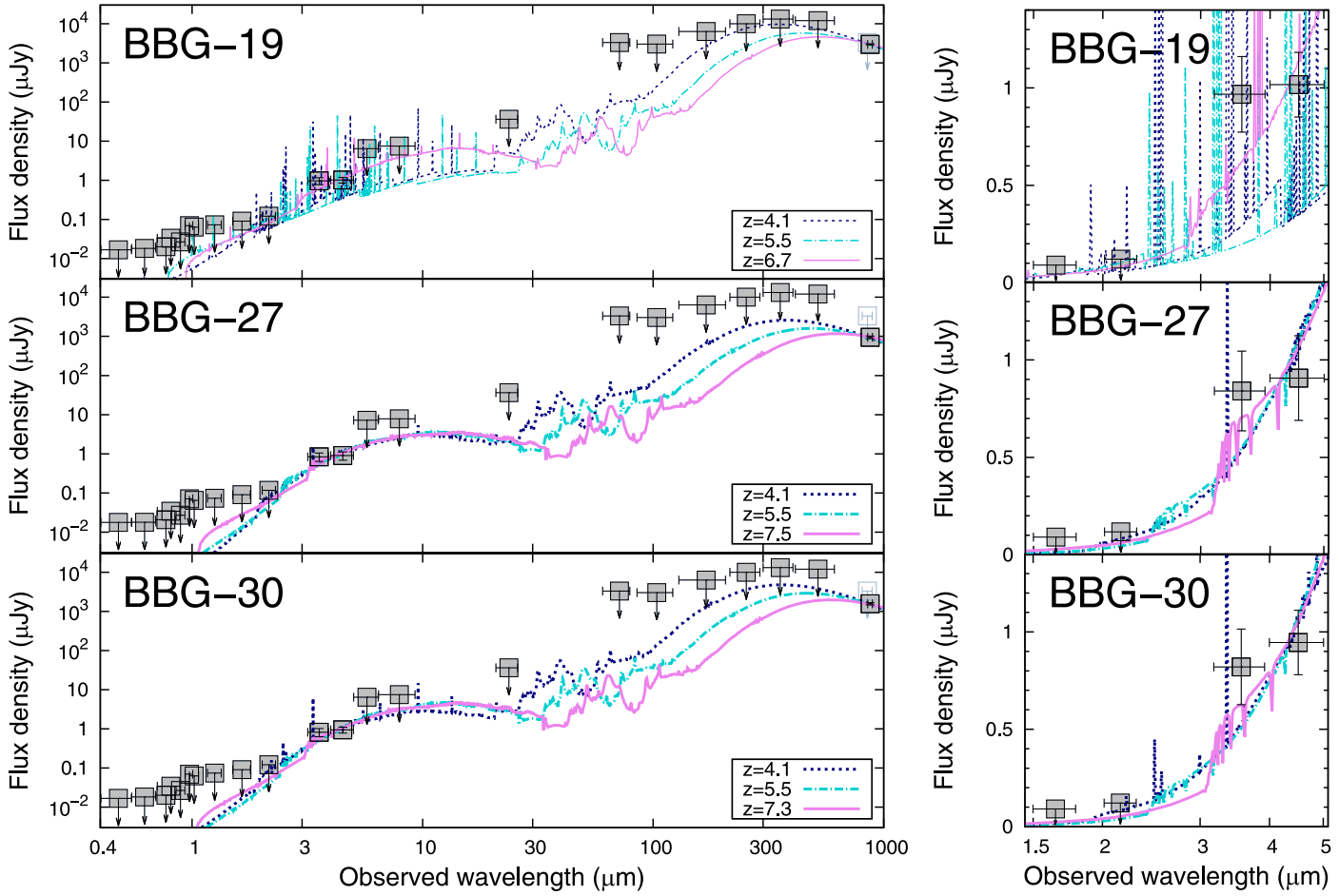

Figure 16. Observed SEDs of the BBG candidates with ALMA detection, where filled (open) squares correspond to the observed photometry used (excluded) in the template fitting. For the nondetection bands, the 2σ limiting fluxes are set as upper limits, indicated by arrows. The DG/DNLE model spectra at $z \sim 4$ (dotted), 5.5 (dotted–dashed), and 7 (solid) are superposed. All three model spectra can reasonably fit the observed SED, with the $z \sim 7$ model being the best-fit template. The right panels are the same as the left ones but in the NIR wavelength range.

of IR luminosity of $12 \lesssim \log(L_{\rm IR}/L_\odot) \lesssim 12.6$ because of the so-called "negative K correction" (e.g., Blain et al. 2002). Figure 16 shows some DG and DNLE model spectra at different redshifts that reasonably fit the observed SEDs of the three ALMA-detected galaxies. We conclude that the three BBG candidates with ALMA detections are actually ultra-luminous infrared galaxies (ULIRGs) with $L_{\rm IR} > 10^{12}\,L_\odot$ (Lonsdale et al. 2006) at $z \gtrsim 4$. Such massive dusty populations were recently reported by Wang et al. (2019). Future redshift confirmation with deep spectroscopy (e.g., by *JWST* or ALMA) is required to further constrain their physical properties.

ORCID iDs

Ken Mawatari https://orcid.org/0000-0003-4985-0201
Akio K. Inoue https://orcid.org/0000-0002-7779-8677
Takuya Hashimoto https://orcid.org/0000-0002-0898-4038
John Silverman https://orcid.org/0000-0002-0000-6977
Masaru Kajisawa https://orcid.org/0000-0002-1732-6387
Satoshi Yamanaka https://orcid.org/0000-0002-7738-5290
Iary Davidzon https://orcid.org/0000-0002-2951-7519
Peter Capak https://orcid.org/0000-0003-3578-6843
Lihwai Lin https://orcid.org/0000-0001-7218-7407
Bau-Ching Hsieh https://orcid.org/0000-0001-5615-4904
Yoshiaki Taniguchi https://orcid.org/0000-0003-2247-3741
Masayuki Tanaka https://orcid.org/0000-0002-5011-5178
Yuichi Harikane https://orcid.org/0000-0002-6047-430X
Yuma Sugahara https://orcid.org/0000-0001-6958-7856
Seiji Fujimoto https://orcid.org/0000-0001-7201-5066
Tohru Nagao https://orcid.org/0000-0002-7402-5441

References

Abazajian, K. N., Adelman-McCarthy, J. K., Agüeros, M. A., et al. 2009, ApJS, 182, 543
Aihara, H., AlSayyad, Y., Ando, M., et al. 2019, PASJ, 72, 114
Aihara, H., Arimoto, N., Armstrong, R., et al. 2018, PASJ, 70, S4
Andrews, S. K., Driver, S. P., Davies, L. J. M., et al. 2017, MNRAS, 464, 1569
Antonucci, R. 1993, ARA&A, 31, 473
Asano, R. S., Takeuchi, T. T., Hirashita, H., & Inoue, A. K. 2013, EP&S, 65, 213
Ashby, M. L. N., Willner, S. P., Fazio, G. G., et al. 2013, ApJ, 769, 80
Baldassare, V. F., Reines, A. E., Gallo, E., & Greene, J. E. 2015, ApJL, 809, L14
Barmby, P., Huang, J. S., Ashby, M. L. N., et al. 2008, ApJS, 177, 431
Behroozi, P. S., Wechsler, R. H., & Conroy, C. 2013, ApJ, 770, 57
Bentz, M. C., & Katz, S. 2015, PASP, 127, 67
Berta, S., Lutz, D., Santini, P., et al. 2013, A&A, 551, A100
Bertin, E., & Arnouts, S. 1996, A&AS, 117, 393
Bhatawdekar, R., Conselice, C. J., Margalef-Bentabol, B., & Duncan, K. 2019, MNRAS, 486, 3805
Blain, A. W., Smail, I., Ivison, R. J., Kneib, J. P., & Frayer, D. T. 2002, PhR, 369, 111
Bohlin, R. C., Savage, B. D., & Drake, J. F. 1978, ApJ, 224, 132
Bouwens, R. J., Aravena, M., Decarli, R., et al. 2016, ApJ, 833, 72

Bouwens, R. J., Illingworth, G. D., Labbe, I., et al. 2011, Natur, 469, 504
Bouwens, R. J., Illingworth, G. D., Oesch, P. A., et al. 2015, ApJ, 803, 34
Bowman, J. D., Rogers, A. E. E., Monsalve, R. A., Mozdzen, T. J., & Mahesh, N. 2018, Natur, 555, 67
Brammer, G. B., Whitaker, K. E., van Dokkum, P. G., et al. 2009, ApJL, 706, L173
Brinchmann, J., Charlot, S., White, S. D. M., et al. 2004, MNRAS, 351, 1151
Bruzual, G., & Charlot, S. 2003, MNRAS, 344, 1000
Calzetti, D., Armus, L., Bohlin, R. C., et al. 2000, ApJ, 533, 682
Cappelluti, N., Brusa, M., Hasinger, G., et al. 2009, A&A, 497, 635
Caputi, K. I., Dunlop, J. S., McLure, R. J., et al. 2012, ApJL, 750, L20
Ceverino, D., Klessen, R. S., & Glover, S. C. O. 2018, MNRAS, 480, 4842
Chabrier, G. 2003, PASP, 115, 763
Charlot, S., & Fall, S. M. 2000, ApJ, 539, 718
Chen, Y.-M., Tremonti, C. A., Heckman, T. M., et al. 2010, AJ, 140, 445
Civano, F., Marchesi, S., Comastri, A., et al. 2016, ApJ, 819, 62
Cox, A. N. 2000, Allena's Astrophysical Quantities (New York: AIP)
da Cunha, E., Charlot, S., & Elbaz, D. 2008, MNRAS, 388, 1595
Davidzon, I., Ilbert, O., Laigle, C., et al. 2017, A&A, 605, A70
Domínguez Sánchez, H., Pozzi, F., Gruppioni, C., et al. 2011, MNRAS, 417, 900
Draine, B. T. 2011, Physics of the Interstellar and Intergalactic Medium (Princeton, NJ: Princeton Univ. Press)
Duncan, K., Conselice, C. J., Mortlock, A., et al. 2014, MNRAS, 444, 2960
Dunlop, J. S., Cirasuolo, M., & McLure, R. J. 2007, MNRAS, 376, 1054
Ellis, R. S., McLure, R. J., Dunlop, J. S., et al. 2013, ApJL, 763, L7
Fazio, G. G., Hora, J. L., Allen, L. E., et al. 2004, ApJS, 154, 10
Feltre, A., Hatziminaoglou, E., Fritz, J., & Franceschini, A. 2012, MNRAS, 426, 120
Finkelstein, S. L., Ryan, R. E., J. Papovich, C., et al. 2015a, ApJ, 810, 71
Finkelstein, S. L., Song, M., Behroozi, P., et al. 2015b, ApJ, 814, 95
Frayer, D. T., Sanders, D. B., Surace, J. A., et al. 2009, AJ, 138, 1261
Fritz, J., Franceschini, A., & Hatziminaoglou, E. 2006, MNRAS, 366, 767
Furusawa, H., Koike, M., Takata, T., et al. 2018, PASJ, 70, S3
Gardner, J. P., Mather, J. C., Clampin, M., et al. 2006, SSRv, 123, 485
Garn, T., & Best, P. N. 2010, MNRAS, 409, 421
Garn, T., Sobral, D., Best, P. N., et al. 2010, MNRAS, 402, 2017
Geach, J. E., Dunlop, J. S., Halpern, M., et al. 2017, MNRAS, 465, 1789
Gehrels, N. 1986, ApJ, 303, 336
Glazebrook, K., Schreiber, C., Labbé, I., et al. 2017, Natur, 544, 71
Grazian, A., Fontana, A., Santini, P., et al. 2015, A&A, 575, A96
Griffin, M. J., Abergel, A., Abreu, A., et al. 2010, A&A, 518, L3
Harikane, Y., Ouchi, M., Ono, Y., et al. 2016, ApJ, 821, 123
Harikane, Y., Ouchi, M., Ono, Y., et al. 2018, PASJ, 70, S11
Hashimoto, T., Inoue, A. K., Mawatari, K., et al. 2019, PASJ, 71, 71
Hashimoto, T., Laporte, N., Mawatari, K., et al. 2018, Natur, 557, 392
Holland, W. S., Bintley, D., Chapin, E. L., et al. 2013, MNRAS, 430, 2513
Hopkins, A. M., & Beacom, J. F. 2006, ApJ, 651, 142
Hopkins, P. F., Wetzel, A., Kereš, D., et al. 2018, MNRAS, 480, 800
Huang, J.-S., Zheng, X. Z., Rigopoulou, D., et al. 2011, ApJL, 742, L13
Inoue, A. K. 2011, MNRAS, 415, 2920
Inoue, A. K., Shimizu, I., Iwata, I., & Tanaka, M. 2014, MNRAS, 442, 1805
Ishigaki, M., Kawamata, R., Ouchi, M., et al. 2018, ApJ, 854, 73
Kajisawa, M., Ichikawa, T., Yoshikawa, T., et al. 2011, PASJ, 63, 403
Kawanomoto, S., Uraguchi, F., Komiyama, Y., et al. 2018, PASJ, 70, 66
Kennicutt, R. C., Jr. 1998, ApJ, 498, 541
Kikuchihara, S., Ouchi, M., Ono, Y., et al. 2019, arXiv:1905.06927
Koekemoer, A. M., Aussel, H., Calzetti, D., et al. 2007, ApJS, 172, 196
Komatsu, E., Smith, K. M., Dunkley, J., et al. 2011, ApJS, 192, 18
Komiyama, Y., Obuchi, Y., Nakaya, H., et al. 2018, PASJ, 70, S2
Laigle, C., McCracken, H. J., Ilbert, O., et al. 2016, ApJS, 224, 24
Le Floc'h, E., Aussel, H., Ilbert, O., et al. 2009, ApJ, 703, 222
Leauthaud, A., Tinker, J., Bundy, K., et al. 2012, ApJ, 744, 159
Leitherer, C., Schaerer, D., Goldader, J. D., et al. 1999, ApJS, 123, 3
Lonsdale, C. J., Farrah, D., & Smith, H. E. 2006, in Ultraluminous Infrared Galaxies, ed. J. W. Mason (Berlin: Springer), 285
Lutz, D., Poglitsch, A., Altieri, B., et al. 2011, A&A, 532, A90
Ma, X., Hopkins, P. F., Garrison-Kimmel, S., et al. 2018, MNRAS, 478, 1694
Madau, P. 2018, MNRAS, 480, L43
Madau, P., & Dickinson, M. 2014, ARA&A, 52, 415
Magnelli, B., Lutz, D., Santini, P., et al. 2012, A&A, 539, A155
Makiya, R., Enoki, M., Ishiyama, T., et al. 2016, PASJ, 68, 25
Mancini, C., Matute, I., Cimatti, A., et al. 2009, A&A, 500, 705
Mawatari, K., Yamada, T., Fazio, G. G., Huang, J.-S., & Ashby, M. L. N. 2016, PASJ, 68, 46
McCracken, H. J., Milvang-Jensen, B., Dunlop, J., et al. 2012, A&A, 544, A156
McLeod, D. J., McLure, R. J., & Dunlop, J. S. 2016, MNRAS, 459, 3812
Merlin, E., Fortuni, F., Torelli, M., et al. 2019, MNRAS, 490, 3309
Miyazaki, S., Komiyama, Y., Kawanomoto, S., et al. 2018, PASJ, 70, S1
Mo, H., van den Bosch, F. C., & White, S. 2010, Galaxy Formation and Evolution (Cambridge: Cambridge Univ. Press)
Mo, H. J., & White, S. D. M. 2002, MNRAS, 336, 112
Mobasher, B., Dickinson, M., Ferguson, H. C., et al. 2005, ApJ, 635, 832
Muzzin, A., Marchesini, D., Stefanon, M., et al. 2013, ApJ, 777, 18
Nayyeri, H., Mobasher, B., Hemmati, S., et al. 2014, ApJ, 794, 68
Oesch, P. A., Bouwens, R. J., Illingworth, G. D., et al. 2012, ApJ, 745, 110
Oesch, P. A., Bouwens, R. J., Illingworth, G. D., et al. 2013, ApJ, 773, 75
Oesch, P. A., Bouwens, R. J., Illingworth, G. D., et al. 2014, ApJ, 786, 108
Oesch, P. A., Bouwens, R. J., Illingworth, G. D., Labbé, I., & Stefanon, M. 2018, ApJ, 855, 105
Oke, J. B., & Gunn, J. E. 1983, ApJ, 266, 713
Oliver, S. J., Bock, J., Altieri, B., et al. 2012, MNRAS, 424, 1614
Phillipps, S. 2005, The Structure and Evolution of Galaxies (Weinheim: Wiley-VCH)
Pilbratt, G. L., Riedinger, J. R., Passvogel, T., et al. 2010, A&A, 518, L1
Poglitsch, A., Waelkens, C., Geis, N., et al. 2010, A&A, 518, L2
Polletta, M., Tajer, M., Maraschi, L., et al. 2007, ApJ, 663, 81
Prevot, M. L., Lequeux, J., Maurice, E., Prevot, L., & Rocca-Volmerange, B. 1984, A&A, 132, 389
Price, S. H., Kriek, M., Brammer, G. B., et al. 2014, ApJ, 788, 86
Rachford, B. L., Snow, T. P., Destree, J. D., et al. 2009, ApJS, 180, 125
Reddy, N. A., & Steidel, C. C. 2009, ApJ, 692, 778
Reines, A. E., & Volonteri, M. 2015, ApJ, 813, 82
Rieke, G. H., Alonso-Herrero, A., Weiner, B. J., et al. 2009, ApJ, 692, 556
Rigopoulou, D., Mainieri, V., Almaini, O., et al. 2009, MNRAS, 400, 1199
Rodighiero, G., Cimatti, A., Franceschini, A., et al. 2007, A&A, 470, 21
Rowan-Robinson, M., Oliver, S., Wang, L., et al. 2016, MNRAS, 461, 1100
Rowlands, K., Dunne, L., Maddox, S., et al. 2012, MNRAS, 419, 2545
Rowlands, K., Gomez, H. L., Dunne, L., et al. 2014, MNRAS, 441, 1040
Sanders, D. B., Salvato, M., Aussel, H., et al. 2007, ApJS, 172, 86
Santini, P., Merlin, E., Fontana, A., et al. 2019, MNRAS, 486, 560
Sawicki, M. 2012, PASP, 124, 1208
Schinnerer, E., Smolčić, V., Carilli, C. L., et al. 2007, ApJS, 172, 46
Schlegel, D. J., Finkbeiner, D. P., & Davis, M. 1998, ApJ, 500, 525
Schmidt, M. 1959, ApJ, 129, 243
Schreiber, C., Labbé, I., Glazebrook, K., et al. 2018, A&A, 611, A22
Scoville, N., Aussel, H., Brusa, M., et al. 2007, ApJS, 172, 1
Seaton, M. J. 1979, MNRAS, 187, 73P
Shen, S., Mo, H. J., White, S. D. M., et al. 2003, MNRAS, 343, 978
Smolčić, V., Novak, M., Delvecchio, I., et al. 2017, A&A, 602, A6
Song, M., Finkelstein, S. L., Ashby, M. L. N., et al. 2016, ApJ, 825, 5
Speagle, J. S., Steinhardt, C. L., Capak, P. L., & Silverman, J. D. 2014, ApJS, 214, 15
Stach, S. M., Dudzevičiūtė, U., Smail, I., et al. 2019, MNRAS, 487, 4648
Straatman, C. M. S., Labbé, I., Spitler, L. R., et al. 2014, ApJL, 783, L14
Sullivan, M., Mobasher, B., Chan, B., et al. 2001, ApJ, 558, 72
Tamura, Y., Mawatari, K., Hashimoto, T., et al. 2019, ApJ, 874, 27
Tanaka, M., Valentino, F., Toft, S., et al. 2019, ApJL, 885, L34
Tody, D. 1986, Proc. SPIE, 627, 733
Tody, D. 1993, in ASP Conf. Ser. 52, Astronomical Data Analysis Software and Systems II, ed. R. J. Hanisch, R. J. V. Brissenden, & J. Barnes (San Francisco, CA: ASP), 173
Trebitsch, M., Blaizot, J., Rosdahl, J., Devriendt, J., & Slyz, A. 2017, MNRAS, 470, 224
Urry, C. M., & Padovani, P. 1995, PASP, 107, 803
Wang, T., Schreiber, C., Elbaz, D., et al. 2019, Natur, 572, 211
Wiklind, T., Dickinson, M., Ferguson, H. C., et al. 2008, ApJ, 676, 781
Williams, R. J., Quadri, R. F., Franx, M., van Dokkum, P., & Labbé, I. 2009, ApJ, 691, 1879
Woo, J.-H., & Urry, C. M. 2002, ApJ, 579, 530